

# Interplay of scales during the spatial evolution of energy-containing motions in wall-bounded turbulent flows

Ezhilsabareesh Kannadasan<sup>1,†</sup>, Callum Atkinson<sup>1</sup> and Julio Soria<sup>1</sup>

<sup>1</sup>Laboratory for Turbulence Research in Aerospace and Combustion (LTRAC), Department of Mechanical and Aerospace Engineering, Monash University, Clayton, Victoria 3800, Australia

(Received 14 June 2023; revised 29 December 2023; accepted 5 March 2024)

This article extends the previous investigation of the spatial evolution of energy-containing motions in wall-bounded turbulent flows (Kannadasan *et al.*, *J. Fluid Mech.*, vol. 955, 2023, R1) by examining their scale-interactions through spectral analysis based on the spanwise scale decomposition of turbulent kinetic energy and the Reynolds stress transport equation. The energy-containing motions located at the inflow of a turbulent channel flow are artificially removed and the interscale transport mechanisms involved in their spatial evolution are studied. This scale interaction analysis reveals the presence of a significant inverse transfer of streamwise Reynolds stress from the near-wall streaks to larger scales in the spatial evolution of energy-containing motions. This transfer is due to the spanwise variation of streamwise velocity fluctuations, represented by  $\partial u' / \partial z$ , which is the primary mechanism of streak instability. The analysis presented in this study also shows that the inverse cascade of spanwise energy may correspond to the regeneration of streamwise vortices in the process of reactivating the self-sustaining mechanism in the spatial evolution of energy-containing motions.

**Key words:** turbulence simulation, turbulence theory, turbulent boundary layers

## 1. Introduction

Energy-containing motions play a pivotal role in the generation of a complex and intricate hierarchy of scale interactions and energy cascade within wall turbulence, thereby sustaining the turbulent flows bounded by walls. These dominant flow features carry most of the kinetic energy and momentum, contributing to the transport and distribution of energy within the turbulent flow. Within the energy-containing motions, coherent

† Email address for correspondence: [ezhilsabareesh.kannadasan@monash.edu](mailto:ezhilsabareesh.kannadasan@monash.edu)

structures, such as streaks and rolls/vortices, have been subject to extensive observation and study since the experiments conducted by Klebanoff, Tidstrom & Sargent (1962), Kline *et al.* (1967) and Kim, Kline & Reynolds (1971). A comprehensive understanding of these coherent structures is crucial for unravelling the intricate mechanisms governing wall-bounded turbulence and advancing our knowledge of wall-bounded turbulent flows in general.

A conceptual model for wall-bounded turbulence, proposed by Townsend (1980), provides insights into the characteristics of energy-containing motions. Townsend deduced that the size of these motions, spanning from the inner viscous scales to the outer length scales, is proportional to their distance from the wall. Moreover, it was explained in the work of Perry & Chong (1982) that these motions exhibit a hierarchical structure.

Numerous studies have focused on isolating and understanding these energy-containing motions, contributing to our comprehension of the spatial organisation of wall turbulence. In particular, energy-containing motions in the buffer layer are involved in a quasi-periodic self-sustaining cycle that plays a crucial role in the maintenance of shear-driven turbulence (Kim *et al.* 1971; Jiménez & Moin 1991; Butler & Farrell 1993; Hamilton, Kim & Waleffe 1995; Schoppa & Hussain 2002). This self-sustaining process is based on the emergence of streaks from wall-normal ejections of fluid (Landahl 1975), followed by their meandering and breakdown (Swearingen & Blackwelder 1987; Waleffe 1995, 1997; Schoppa & Hussain 2002). The cycle is restarted by the generation of new vortices from the perturbations created by the disrupted streaks. The interdependence of vortices and streaks in the self-sustaining cycle of wall-bounded turbulence was demonstrated by previous studies, which have shown that damping out either of them inevitably interrupts the turbulence cycle (Jiménez & Pinelli 1999). The large-scale energy-containing motions further away from the wall within the logarithmic layer are also expected to be self-sustaining, albeit in a more disorganised manner (Flores & Jiménez 2006; Flores, Jiménez & Del Alamo 2007; Hwang & Cossu 2010).

While the classical perspective of wall-bounded turbulence states that energy-containing motions are self-sustaining at each relevant length scale, the interactions between these energy-containing motions remain significant. In the near-wall region, the interaction between wall-attached eddies plays a vital role in generating skin friction (de Giovanetti, Hwang & Choi 2016). Additionally, large-scale motions in the outer layer have a modulating effect, called amplitude modulation, on the magnitude of small-scale events in the near-wall region (Hutchins & Marusic 2007; Dogan *et al.* 2019). This modulating effect increases with the Reynolds number (Mathis, Hutchins & Marusic 2009).

The multi-scale interactions of energy-containing motions have recently garnered interest within the fluids community, and there have been intensive efforts to study the interscale energy transfer (Cimarelli, De Angelis & Casciola 2013; Hamba 2015; Cimarelli *et al.* 2016; Mizuno 2016; Cho, Hwang & Choi 2018; Kawata & Alfredsson 2018; Bauer, von Kameke & Wagner 2019; Lee & Moser 2019; Motoori & Goto 2021). Interestingly, some studies have noted from the spectral analysis of the Reynolds stress transport equation (RSTE) that energy transfer from large to small scales is accompanied by an inverse transfer from small to large scales (Mizuno 2016; Lee & Moser 2019), i.e. opposite from the classical Richardson–Kolmogorov energy cascade (Richardson 1922). Moreover, scale-interaction studies have observed that such an inverse energy cascade is predominantly found only in the streamwise and spanwise velocity components (Cho *et al.* 2018; Lee & Moser 2019; Kawata & Tsukahara 2021). In fact, the interscale transport mechanisms can be directly related to the different components of the self-sustaining cycle. For example, the recent study of Kawata & Tsukahara (2021) conjectured that the forward and inverse energy cascades primarily characterise the streak instabilities and

regeneration of streamwise vortices, respectively. The aforementioned studies are based on fully developed wall-bounded turbulent flows, in which the energy-containing motions are involved in a temporal self-sustaining cycle. However, the interscale transport mechanisms behind the spatial evolution of energy-containing motions remain unclear.

In an attempt to investigate the spatial evolution of energy-containing motions, Kannadasan, Atkinson & Soria (2023) demonstrated that the formation of near-wall streaks is the primary process in the recovery of energy-containing motions. However, the role of interscale energy transport mechanisms in the formation of energy-containing motions at different length scales and the re-establishment of the self-sustaining process remains an unanswered question. In this paper, the interscale transport of turbulent kinetic energy (TKE) and Reynolds stresses in the streamwise development of energy-containing motions is investigated using the framework of Kawata & Alfredsson (2018) to study the interscale energy transfer processes in a spatially evolving turbulent channel flow. The manuscript is structured as follows. Section 2 provides details on the numerical experiments. The methodology for isolating energy-containing motions is outlined in § 2.1, while § 2.2 summarises the interscale transport equations. Moving on to § 3, one-dimensional velocity and vorticity spectra are presented in §§ 3.1 and 3.2, respectively. The mean momentum balance, TKE budget and Reynolds stress budget of the spatially evolving inflow-outflow boundary conditions DNS (IOCH-DNS) are discussed in §§ 3.3, 3.4 and 3.5, respectively. Further analyses include spectral examination of TKE production in § 3.6 and inter-component energy transfer in § 3.7. Interscale transfer of TKE and Reynolds stresses is addressed in §§ 3.8 and 3.9. The manuscript concludes with a summary in § 4.

## 2. Numerical experiments

The spatial evolution of energy-containing motions is examined by performing direct numerical simulation (DNS) of incompressible turbulent flow in a plane channel. Hereafter, the streamwise, wall-normal and spanwise directions will be denoted as  $x$ ,  $y$  and  $z$ , respectively, with corresponding velocity components  $u$ ,  $v$  and  $w$ . A fractional-step method (Kim & Moin 1985) is used to solve the incompressible Navier–Stokes equations with a staggered, second-order, finite-difference scheme. The equations are advanced in time using a third-order Runge–Kutta scheme. The channel flow is simulated with the number of grid points  $N_x$ ,  $N_y$  and  $N_z$  in the streamwise, wall-normal and spanwise directions, respectively, and the size of the computational domain in the respective directions denoted by  $L_x$ ,  $L_y$  and  $L_z$ . The DNS code has been validated in previous studies of turbulent channel flow (Lozano-Durán & Bae 2019) and flat-plate boundary layer flow (Lozano-Durán, Hack & Moin 2018). The present DNS was performed at a frictional Reynolds number,  $Re_\tau = 550$ , with the grid properties listed in table 1. The grid spacing in the streamwise,  $\Delta x^+$ , and spanwise directions,  $\Delta z^+$ , is constant. The minimum wall-normal grid spacing is located adjacent to the walls,  $\Delta y_{min}^+$ , with the maximum wall-normal grid spacing located at the channel centreline,  $\Delta y_{max}^+$ . The ‘+’ superscript denotes wall units defined from the viscous length scale  $\nu/u_\tau$ . A constant time-step size was used for the present DNS given non-dimensionalised as  $\Delta t^+ = \Delta t u_\tau^2 / \nu$  in table 1.

The present study uses two synchronised DNS: a fully resolved streamwise periodic channel flow, referred to as PCH-DNS, and a fully resolved channel flow DNS with inflow-outflow boundary conditions, referred to as IOCH-DNS. In the IOCH-DNS, the inlet boundary condition is a filtered version of the inflow of PCH-DNS, and a convective outflow boundary condition is applied at the domain exit. Figure 1 shows a schematic of the

$Re_\tau$	$L_x/h$	$L_z/h$	$N_x$	$N_y$	$N_z$	$\Delta x^+$	$\Delta y_{min}^+$	$\Delta y_{max}^+$	$\Delta z^+$	$\Delta t^+$
550	$8\pi$	$\pi$	1560	456	384	6.65	0.31	2.87	3.36	0.11

Table 1. DNS numerical details including domain size and grid spacing for both the PCH- and IOCH-DNS.

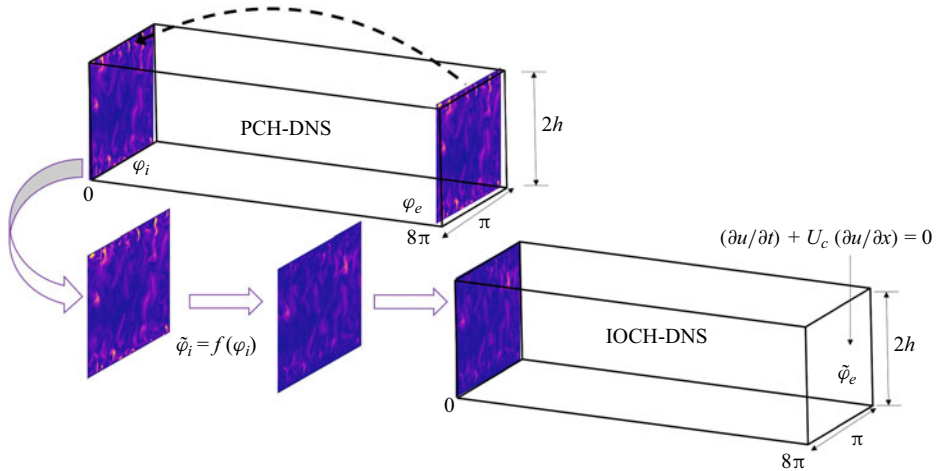


Figure 1. Schematic diagram illustrating the generation of the filtered velocity inflow boundary condition for IOCH-DNS. Here,  $\tilde{\varphi}$  represents the inlet and outlet planes of the IOCH-DNS,  $f(\varphi)$  denotes the filtering of the velocity field, and  $U_c$  is the centreline velocity.

computational set-up, which is divided into two DNS with different inlet/outlet boundary conditions. The first DNS is a fully resolved streamwise periodic channel flow DNS (PCH-DNS), with planes  $\varphi_i$  and  $\varphi_e$  representing the inlet and outlet planes, respectively. The outlet plane  $\varphi_e$  is recycled back to the inlet to ensure streamwise periodicity. The second DNS is a fully resolved channel flow DNS with inflow-outflow boundary conditions (IOCH-DNS), with plane  $\tilde{\varphi}_i$  serving as the inflow boundary condition, where  $\tilde{\varphi}_i$  denotes filtering of the inlet plane and the outlet plane of the IOCH-DNS is referred as  $\tilde{\varphi}_e$ , where the convective boundary condition is applied. Once the initial transients of the IOCH-DNS are washed out, the statistics of the IOCH-DNS are accumulated until it reaches a statistically stationary state. It is to be noted that a constant pressure gradient is imposed in both the PCH-DNS and IOCH-DNS, which results in a constant momentum flux in the simulations.

To validate the methodology of IOCH-DNS, fully resolved inflow data from PCH-DNS were used as the inflow boundary condition for  $Re_\tau = 550$ . First- and second-order statistics for the entire IOCH-DNS flow field were compared with those of the PCH-DNS and previous turbulent channel flow DNS of Hoyas & Jiménez (2008). The results, shown in figure 2(a,b), demonstrate that the mean velocity and fluctuating velocity profiles of IOCH-DNS are identical to those of PCH-DNS. The premultiplied spectrum of the streamwise velocity, represented by  $k_z \phi_{uu}$ , is shown in figure 2(c) and visualises the energy density distribution of the streamwise velocity fluctuations across different wavelengths. Time-averaged and streamwise-averaged  $k_z \phi_{uu}$  spectra demonstrate that the IOCH-DNS effectively replicates the energy distribution across all scales, akin to those of the PCH-DNS.

## Interplay of scales of energy-containing motions

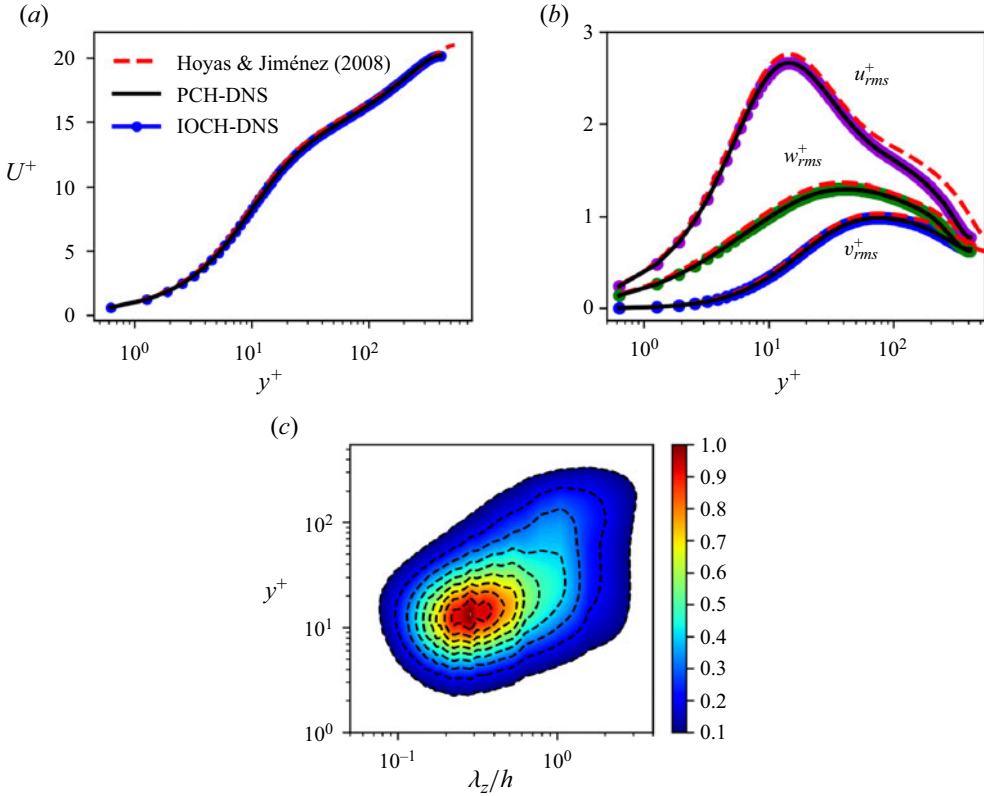


Figure 2. Validation of IOCH-DNS with PCH-DNS and DNS of Hoyas & Jiménez (2008) at  $Re_\tau = 550$ : (a) mean velocity profile; (b) root-mean-squared velocity profiles; (c) premultiplied spanwise spectra of the streamwise velocity,  $k_z \phi_{uu}$ , as a function of  $y^+$  – the contours are equally spaced between 0.1 and 1.0 of the maximum value of  $k_z \phi_{uu}$  of the PCH-DNS; PCH-DNS (black dashed line), IOCH-DNS (colour contour).

### 2.1. Isolating the energy-containing motions

The TKE budget equation is given as

$$\begin{aligned}
 \frac{\partial \langle e \rangle}{\partial t} = & \underbrace{-\langle u'_i u'_j \rangle \frac{\partial \langle u_i \rangle}{\partial x_j}}_P - \underbrace{v \left\langle \frac{\partial u'_i}{\partial x_j} \frac{\partial u'_i}{\partial x_j} \right\rangle}_\epsilon - \underbrace{\frac{1}{2} \frac{\partial \langle u'_i u'_i u'_j \rangle}{\partial x_j}}_{T_{turb}} - \underbrace{\frac{1}{\rho} \frac{\partial \langle p' u'_j \rangle}{\partial x_j}}_{T_p} \\
 & + \underbrace{v \frac{\partial^2 \langle e \rangle}{\partial x_j \partial x_j}}_{T_v} - \underbrace{\langle u_j \rangle \frac{\partial \langle e \rangle}{\partial x_j}}_C, \tag{2.1}
 \end{aligned}$$

where  $'$  denotes the fluctuating component,  $e = (u'^2 + v'^2 + w'^2)/2$  and for the PCH-DNS,  $\langle \cdot \rangle$  denotes the average over time and the homogeneous streamwise and spanwise directions, while for the IOCH-DNS,  $\langle \cdot \rangle$  denotes the average over time and spanwise direction only, since the flow is inhomogeneous, i.e. the flow is spatially developing in the streamwise direction in the IOCH-DNS. The terms labelled  $P$ ,  $\epsilon$ ,  $T_{turb}$ ,  $T_p$ ,  $T_v$  and  $C$  in (2.1) are interpreted as turbulence production, viscous dissipation, turbulent transport, pressure transport, viscous transport and convection, respectively.

Since, the size of the energy-containing motions in wall-bounded turbulence can be characterised by the spanwise length scale (Hwang 2015) and due to the flow inhomogeneity in the streamwise direction of the IOCH-DNS, a Fourier decomposition of the velocity fluctuations in the spanwise direction is considered as follows:

$$u'_i(t, x, y, z) = \int \widehat{u}'_i(t, x, y, k_z) e^{ik_z z} dk_z, \tag{2.2}$$

where  $\widehat{\cdot}$  denotes the Fourier coefficient and  $k_z$  is the spanwise wavenumber with  $\lambda_z = (2\pi)/k_z$  its corresponding spanwise wavelength. The time rate of change of the energy balance equation (2.1) in Fourier space is given as

$$\begin{aligned} \frac{D\widehat{e}(k_z)}{Dt} = & - \underbrace{\left\langle Re \left\{ \widehat{u}'_i^* \widehat{u}'_j \frac{\partial (u_i)}{\partial x_j} \right\} \right\rangle}_{\widehat{P}(y, k_z)} - \underbrace{\left\langle v \frac{\partial \widehat{u}'_i}{\partial x_j} \frac{\partial \widehat{u}'_i^*}{\partial x_j} \right\rangle}_{\widehat{e}(y, k_z)} - \underbrace{\left\langle Re \left\{ \widehat{u}'_i^* \frac{\partial \widehat{u}'_i \widehat{u}'_j}{\partial x_j} \right\} \right\rangle}_{\widehat{T}_{urb}(y, k_z)} \\ & - \underbrace{\left\langle Re \left\{ \frac{1}{\rho} \frac{\partial \widehat{p}' \widehat{u}'_j^*}{\partial x_j} \right\} \right\rangle}_{\widehat{T}_p(y, k_z)} + \underbrace{\left\langle v \frac{\partial^2 \widehat{e}}{\partial x_j \partial x_j} \right\rangle}_{\widehat{T}_v(y, k_z)}, \tag{2.3} \end{aligned}$$

where  $\overline{\cdot}$  denotes the time average, while  $\langle \cdot \rangle$  denotes the spatial average in the streamwise direction only for the PCH-DNS, the superscript  $(\cdot)^*$  denotes the complex conjugate,  $Re\{\cdot\}$  denotes the real part and  $\widehat{e}(k_z) = (|\widehat{u}'(k_z)|^2 + |\widehat{v}'(k_z)|^2 + |\widehat{w}'(k_z)|^2)/2$ . The left-hand side of (2.3) vanishes in a statistically steady flow.

Energy-containing motions are a direct result of turbulence production, manifested across multiple length scales, forming a complex interplay of scale interactions and energy cascades. The motions that originate specifically from the energy cascade process are referred to as energy-cascading motions. The Fourier modes of the turbulent transport term ( $\widehat{T}_{urb}(y, k_z)$ ), resolves not only the energy-containing motions but also those generated by the energy cascade. To identify the boundary that distinguishes the energy-containing motions from the energy-cascading motions, the premultiplied spanwise turbulent transport spectra ( $\widehat{T}_{urb}(y, k_z)$ ) as a function of wall distance need to be considered.

Cho *et al.* (2018)'s investigation of these spanwise spectra of the TKE and the turbulent transport suggested  $\lambda_z = 3y$  as a reasonable boundary that separates the energy-containing motions from the cascading motions. Figure 3 shows the premultiplied spanwise spectra as a function of wall-distance of the turbulent transport ( $k_z^+ y^+ \widehat{T}_{urb}^+$ ) and TKE ( $k_z^+ y^+ \widehat{e}^+$ ) of the PCH-DNS. The TKE spectra contain most of the energy below the ridge  $\lambda_z = 3y$  with the corresponding region in the turbulent transport spectra being negative, which is the donor region in the  $k_z^+ y^+ \widehat{T}_{urb}^+$  spectrum. Therefore, at a given spanwise Fourier mode  $\lambda_{z,0}$ , the wall-normal profile with  $y < \lambda_{z,0}/3$  contains the energy-containing motions and the wall-normal profile with  $y > \lambda_{z,0}/3$  contains the energy-cascading motions. The velocity fluctuations are decomposed into spanwise Fourier modes and, at a given Fourier mode  $\lambda_{z,0}$ , the fluctuations and energy in the wall-normal profile with  $y < \lambda_{z,0}/3$  are removed and only the motions involved in the energy cascade contribute to the inflow velocity field of the IOCH-DNS. It is to be noted that the  $k_z^+ y^+ \widehat{T}_{urb}^+$  spectrum, as depicted in figure 3(a), encompasses both turbulent transport in the wall-normal direction and scale transfer.

## Interplay of scales of energy-containing motions

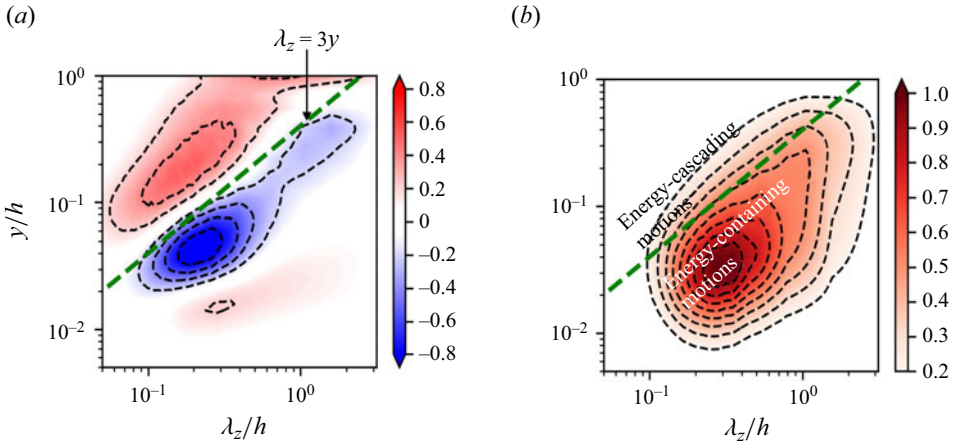


Figure 3. Premultiplied spanwise spectra: (a) turbulent transport ( $k_z^+ y^+ \hat{T}_{turb}^+$ ) and (b) turbulent kinetic energy ( $k_z^+ y^+ \hat{e}$ ) of the PCH-DNS at  $Re_\tau = 550$ . The dashed green line represents  $\lambda_z = 3y$ .

However, the distinction between energy-containing and cascading motions manifests similarly in the spectra of both  $k_z^+ y^+ \hat{T}_{turb}^+$  and the spectrum of interscale transfer (presented in figure 17a) in turbulent channel flows. This similarity, aligned with the findings of Lee & Moser (2019), highlights the dominance of scale transfer over wall-normal transfer in a turbulent channel flow which substantiates the use of a  $k_z^+ y^+ \hat{T}_{turb}^+$  spectrum for identifying energy-containing motions. The filtering operation in the form of spatial convolution is expressed as

$$\tilde{u}_i(0, y, z) = \int G(r, y) u_i(0, y, z - r) dr, \quad (2.4)$$

where  $G(r, y)$  is a filter function. Equation (2.4) can also be written in terms of the spanwise Fourier transform of the filter, the velocity field at the inlet and its filtered version as

$$\hat{\tilde{u}}_i(0, y, k_z) = \hat{G}(y, k_z) \hat{u}_i(0, y, k_z), \quad (2.5)$$

where the spanwise Fourier transform of the filter function  $G(r, y)$  is given as

$$\hat{G}(y, k_z) = \begin{cases} 1 & \text{if } y > \lambda_{z,0}/3, \\ 0 & \text{otherwise.} \end{cases} \quad (2.6)$$

The spatial development of energy-containing motions in the IOCH-DNS is analysed by filtering them at the inflow plane. This filtering process is performed at every time step by using data from the fully resolved PCH-DNS, and employing the filter function detailed in (2.6). The filtered data are then integrated into the IOCH-DNS, as illustrated in figure 1.

### 2.2. Interscale transport equations

Interscale energy transfer is crucial in the formation of energy-containing motions, and scale interaction analysis is required to reveal the complex scale interactions involved in the recovery of energy-containing motions. Kawata & Alfredsson (2018) analysed interscale energy transfer in a plane Couette flow by decomposing fluctuating velocity into large-scale ( $u^{(L)}$ ) and small-scale ( $u^{(S)}$ ) parts in the spanwise wavenumber direction.

The cross-correlation  $\langle u'^{(L)}u'^{(S)} \rangle$  vanishes due to the orthogonal Fourier filter, allowing derivation of transport equations for the large- and small-scale parts of the Reynolds stress transport equation (RSTE). The RSTE budget equation is given as

$$\begin{aligned} \frac{D\langle u'_i u'_j \rangle}{Dt} = & \underbrace{-\langle u'_j u'_k \rangle \frac{\partial \langle u_i \rangle}{\partial x_k} - \langle u'_i u'_k \rangle \frac{\partial \langle u_j \rangle}{\partial x_k}}_{P_{ij}} - 2\nu \underbrace{\left\langle \frac{\partial u'_j}{\partial x_k} \frac{\partial u'_i}{\partial x_k} \right\rangle}_{\epsilon_{ij}} \\ & - \underbrace{\frac{\partial \langle u'_i u'_j u'_k \rangle}{\partial x_k}}_{T_{urb;ij}} - \underbrace{\frac{1}{\rho} \left\langle u'_j \frac{\partial p'}{\partial x_i} + u'_i \frac{\partial p'}{\partial x_j} \right\rangle}_{\Pi_{ij}} + \underbrace{\nu \frac{\partial^2 \langle u'_i u'_j \rangle}{\partial x_k \partial x_k}}_{T_{v;ij}}. \end{aligned} \quad (2.7)$$

The terms denoted by  $P$ ,  $\epsilon$ ,  $T_{urb}$ ,  $\Pi$  and  $T_v$  in (2.7) are identified as the production, viscous dissipation, turbulent transport, pressure-strain and viscous transport components of the RSTE, respectively. The RSTE equation in (2.7) can be decomposed into large- and small-scale parts as  $\langle u'_i u'_j \rangle = \langle u_i'^{(L)} u_j'^{(L)} \rangle + \langle u_i'^{(S)} u_j'^{(S)} \rangle$ , and the decomposed RSTE equations are presented as follows:

$$\begin{aligned} \frac{D\langle u_i'^{(L)} u_j'^{(L)} \rangle}{Dt} = & \underbrace{-\langle u_j'^{(L)} u_k'^{(L)} \rangle \frac{\partial \langle u_i \rangle}{\partial x_k} - \langle u_i'^{(L)} u_k'^{(L)} \rangle \frac{\partial \langle u_j \rangle}{\partial x_k}}_{P_{ij}^L} - 2\nu \underbrace{\left\langle \frac{\partial u_j'^{(L)}}{\partial x_k} \frac{\partial u_i'^{(L)}}{\partial x_k} \right\rangle}_{\epsilon_{ij}^L} \\ & - \frac{1}{\rho} \underbrace{\left\langle u_j'^{(L)} \frac{\partial p'}{\partial x_i} + u_i'^{(L)} \frac{\partial p'}{\partial x_j} \right\rangle}_{\Pi_{ij}^L} + \underbrace{\nu \frac{\partial^2 \langle u_i'^{(L)} u_j'^{(L)} \rangle}{\partial x_k \partial x_k}}_{T_{v;ij}^L} - T_{r;ij} + D_{ij}^{(L)}, \end{aligned} \quad (2.8)$$

$$\begin{aligned} \frac{D\langle u_i'^{(S)} u_j'^{(S)} \rangle}{Dt} = & \underbrace{-\langle u_j'^{(S)} u_k'^{(S)} \rangle \frac{\partial \langle u_i \rangle}{\partial x_k} - \langle u_i'^{(S)} u_k'^{(S)} \rangle \frac{\partial \langle u_j \rangle}{\partial x_k}}_{P_{ij}^S} - 2\nu \underbrace{\left\langle \frac{\partial u_j'^{(S)}}{\partial x_k} \frac{\partial u_i'^{(S)}}{\partial x_k} \right\rangle}_{\epsilon_{ij}^S} \\ & - \frac{1}{\rho} \underbrace{\left\langle u_j'^{(S)} \frac{\partial p'}{\partial x_i} + u_i'^{(S)} \frac{\partial p'}{\partial x_j} \right\rangle}_{\Pi_{ij}^S} + \underbrace{\nu \frac{\partial^2 \langle u_i'^{(S)} u_j'^{(S)} \rangle}{\partial x_k \partial x_k}}_{T_{v;ij}^L} - T_{r;ij} + D_{ij}^{(S)}, \end{aligned} \quad (2.9)$$

where  $T_{r;ij}$  represents the interscale flux of the Reynolds stress from the large- to small-scale across the cutoff wavenumber  $k_z$ , and the terms  $D_{ij}^{(kt,L)}$  and  $D_{ij}^{(kt,S)}$  correspond to the turbulent spatial redistribution of  $u_i'^{(L)} u_j'^{(L)}$  and  $u_i'^{(S)} u_j'^{(S)}$ , respectively. The spatial and interscale turbulent transport of Reynolds stress can be described by the decomposed

RSTE equations given as

$$D_{ij}^{(L)} = -\frac{\partial}{\partial x_k} (\langle u_i'^{(L)} u_j'^{(L)} u_k'^{(L)} \rangle + \langle u_i'^{(L)} u_j'^{(L)} u_k'^{(S)} \rangle + \langle u_i'^{(S)} u_j'^{(L)} u_k'^{(S)} \rangle + \langle u_i'^{(L)} u_j'^{(S)} u_k'^{(S)} \rangle), \quad (2.10a)$$

$$D_{ij}^{(S)} = -\frac{\partial}{\partial x_k} (\langle u_i'^{(S)} u_j'^{(S)} u_k'^{(S)} \rangle + \langle u_i'^{(S)} u_j'^{(S)} u_k'^{(L)} \rangle + \langle u_i'^{(L)} u_j'^{(S)} u_k'^{(L)} \rangle + \langle u_i'^{(S)} u_j'^{(L)} u_k'^{(L)} \rangle), \quad (2.10b)$$

$$T_{r_{ij}} = -\left\langle u_i'^{(S)} u_k'^{(S)} \frac{\partial u_j'^{(L)}}{\partial x_k} \right\rangle - \left\langle u_j'^{(S)} u_k'^{(S)} \frac{\partial u_i'^{(L)}}{\partial x_k} \right\rangle + \left\langle u_i'^{(L)} u_k'^{(L)} \frac{\partial u_j'^{(S)}}{\partial x_k} \right\rangle + \left\langle u_j'^{(L)} u_k'^{(L)} \frac{\partial u_i'^{(S)}}{\partial x_k} \right\rangle. \quad (2.10c)$$

The turbulent interscale transport term,  $T_{r_{ij}}$ , describes the flux of Reynolds stress from the large-scale to the small-scale components across the cutoff wavenumber  $k_z$ . Analogous to Reynolds stress production in (2.7), the first two terms in (2.10c) represent the Reynolds stress transfer from the large to small scales, while the last two terms denote the transfer from small to large scales. To obtain the scale-by-scale transport of Reynolds stress, (2.10c) is differentiated with respect to  $k_z$ . Thus, the scale-by-scale transport of Reynolds stress is defined as

$$t_{r_{ij}} = -\frac{\partial T_{r_{ij}}}{\partial k_z}. \quad (2.11)$$

The derivatives of  $T_{r_{ij}}$  with respect to  $k_z$  in (2.11) indicate the local gain or loss of kinetic energy at  $k_z$  due to interscale flux.

The TKE budget equation, as expressed in (2.1), can be segmented into large- and small-scale components, akin to the decomposition of the Reynolds stress transport equations (RSTEs) seen in (2.8) and (2.9). The decomposed TKE budget equation retains similar production, viscous transport, pressure transport and dissipation terms as the original TKE budget equation. The primary distinction in the decomposed version lies in the turbulent transport term, which bifurcates into two segments: the turbulent spatial transport components  $D_{ij}^{(kt,L)}$  and  $D_{ij}^{(kt,S)}$ , and the interscale turbulent transport term  $T_{r_{ij}}^{kt}$ . These components parallel the turbulent transport terms of RSTE given in (2.10c). The spatial and interscale turbulent transport terms of the TKE budget equation (2.1) are derived by contracting the indices of the spatial and interscale turbulent transport terms of the RSTE presented in (2.10), with the equations detailed as follows:

$$D_{ij}^{(kt,L)} = -\frac{1}{2} \frac{\partial}{\partial x_j} \left( \langle u_i'^{(L)} u_i'^{(L)} u_j'^{(L)} \rangle + \langle u_i'^{(L)} u_i'^{(L)} u_j'^{(S)} \rangle + \langle u_i'^{(S)} u_i'^{(L)} u_j'^{(S)} \rangle + \langle u_i'^{(L)} u_i'^{(S)} u_j'^{(S)} \rangle \right), \quad (2.12a)$$

$$D_{ij}^{(kt,S)} = -\frac{1}{2} \frac{\partial}{\partial x_j} \left( \langle u_i'^{(S)} u_i'^{(S)} u_j'^{(S)} \rangle + \langle u_i'^{(S)} u_i'^{(S)} u_j'^{(L)} \rangle + \langle u_i'^{(L)} u_i'^{(S)} u_j'^{(L)} \rangle + \langle u_i'^{(S)} u_i'^{(L)} u_j'^{(L)} \rangle \right), \quad (2.12b)$$

$$T_{r_{ij}}^{kt} = -2 \left\langle u_i'^{(S)} u_j'^{(S)} \frac{\partial u_i'^{(L)}}{\partial x_j} \right\rangle + 2 \left\langle u_i'^{(L)} u_j'^{(L)} \frac{\partial u_i'^{(S)}}{\partial x_j} \right\rangle. \quad (2.12c)$$

The interscale transport of TKE at each scale is derived by differentiating  $T_{r_{ij}}^{kt}$  from (2.12c) with respect to the spanwise cutoff wavenumber  $k_z$ :

$$t_{r_{ij}}^{kt} = -\frac{\partial T_{r_{ij}}^{kt}}{\partial k_z}. \quad (2.13)$$

### 3. Results and discussions

#### 3.1. One-dimensional velocity spectra

The velocity spectra of the spatially evolving IOCH-DNS, as previously highlighted by Kannadasan *et al.* (2023), are succinctly addressed here to ensure the comprehensiveness of this paper, with particular emphasis on the streamwise velocity spectra. The streamwise velocity spectra  $k_z \phi_{uu}$  of the IOCH-DNS in figure 4 explicitly show that eliminating near-wall energy-containing motions at the inflow results in a consequential decay in energy-cascade motions. As the flow advances downstream, there is a significant reduction in the streamwise energy above the cutoff ridge of  $\lambda_z = 3y$ , signifying the decay of energy-cascade motions in the absence of energy-containing motions. In the early stages of evolution, the streamwise velocity spectra,  $k_z \phi_{uu}$ , begin to recover energy below the ridge  $\lambda_z = 3y$  at a spanwise length scale of  $\lambda_z^+ \approx 100$ , as shown in figure 4(b–d). This scale corresponds closely with the typical spanwise spacing of near-wall streaks.

Furthermore, in the IOCH-DNS, as the streamwise velocity spectra evolve, there is a noticeable decay in the wall-normal ( $k_z \phi_{vv}$ ) and spanwise ( $k_z \phi_{ww}$ ) velocity spectra for  $x < 6h$ , as discussed by Kannadasan *et al.* (2023). This decay, mostly seen above the ridge  $\lambda_z = 3y$ , signifies the weakening of energy-cascade motions without the energy-containing motions. However,  $k_z \phi_{vv}$  and  $k_z \phi_{ww}$  spectra begin to recover for  $x > 6h$  through the redistribution of the streamwise turbulent energy once the near-wall peak of the  $k_z \phi_{uu}$  spectrum is recovered and re-established. These observations are in line with typical transitions to turbulence, where the streaks are generated by extracting the energy from the mean flow and the wall-normal and spanwise velocity components decay while activating the long streaks in the flow (Landahl 1975; Butler & Farrell 1993), making them prominent early in the spatial evolution of energy-containing motions. Particularly, the near-wall streak amplitude in the  $k_z \phi_{uu}$  spectrum is higher than the PCH-DNS, as shown in figure 4(b–d). This suggests a likely streak breakdown beyond  $x > 6h$ , initiating a self-sustaining cycle. This sequence resembles the ‘bypass transition’ in turbulent boundary layers, even when the underlying mean velocity remains turbulent in the IOCH-DNS. For more details on the fluctuating velocity statistics and spectra of the IOCH-DNS, readers are encouraged to refer to the work of Kannadasan *et al.* (2023).

#### 3.2. One-dimensional vorticity spectra

Figure 5(a) presents the evolution of streamwise vorticity spectra ( $k_z \phi_{\omega_x \omega_x}$ ) in the IOCH-DNS alongside the fully developed spectrum from the PCH-DNS for comparison. The PCH-DNS spectrum features two prominent peaks: a near-wall peak at  $y^+ \simeq 1 \sim 5$  and another within the buffer layer at  $y^+ \simeq 20$ . As the flow develops in the streamwise direction, there is no evidence of active vortical motions for  $x \leq 6h$ , as shown in figure 5

*Interplay of scales of energy-containing motions*

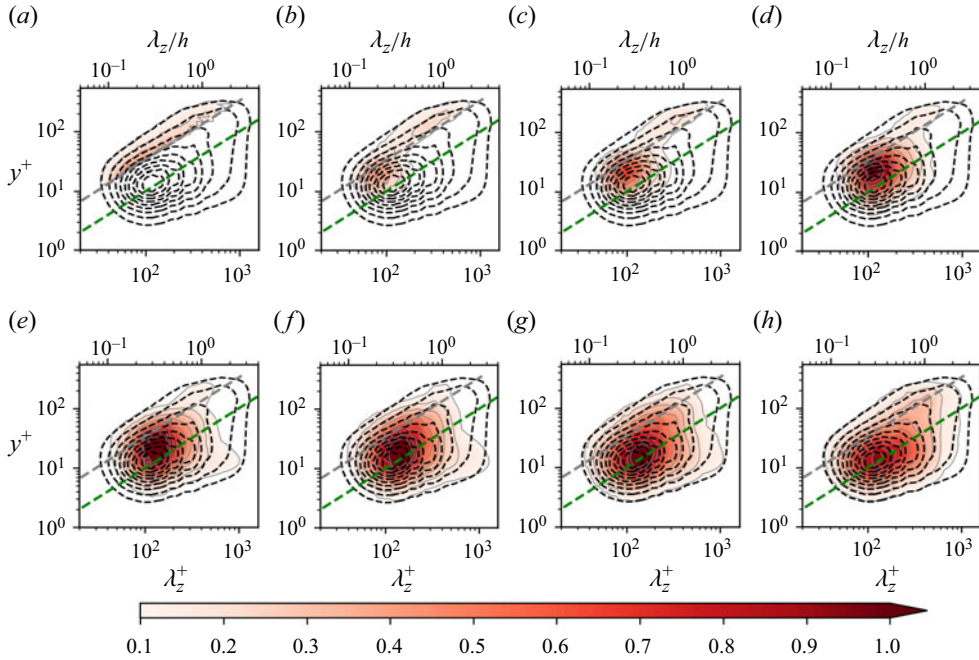


Figure 4. Premultiplied spanwise spectra of the streamwise velocity,  $k_z \phi_{uu}$ , as a function of  $y$  at various streamwise locations: (a)  $x = 0h$ ; (b)  $x = 1.5h$ ; (c)  $x = 3h$ ; (d)  $x = 6h$ ; (e)  $x = 8h$ ; (f)  $x = 10h$ ; (g)  $x = 12h$ ; (h)  $x = 24h$ . The contours are 0.1 to 1.0 of the maximum value of  $k_z \phi_{uu}$  of the PCH-DNS; PCH-DNS (black dashed line), IOCH-DNS (contour enclosed in the grey line). Here, grey dashed line is at  $\lambda_z = 3y$  to indicate the cutoff spanwise wavelength and the green dashed line is at  $\lambda_z = 10y$ .

at  $x = 1.5, 3$  and  $6h$ , where the  $k_z \phi_{uu}$  spectrum has not yet fully recovered its energy at the spanwise wavelength equivalent to the spacing of the near-wall streaks. The activation of vortical motions is observed beyond  $x = 6h$ , where the near-wall peak of the  $k_z \phi_{uu}$  spectrum approaches complete recovery, suggesting a reactivation of the streamwise vortical structures concurrent with the re-establishment of near-wall streaks.

In contrast, the premultiplied spanwise energy spectra of wall-normal vorticity fluctuations ( $k_z \phi_{\omega_y \omega_y}$ ) depicted in figure 5(b) shows active wall-normal vortical motions in the early stages of streamwise evolution of energy-containing motions, which is consistent with the streamwise velocity spectra  $k_z \phi_{uu}$  and aligns with the streak formation, corroborating the presence of strong wall-normal vorticity at the streak edges as described by Kim (2011).

The premultiplied spanwise energy spectra of spanwise vorticity fluctuations ( $k_z \phi_{\omega_z \omega_z}$ ) is shown in figure 5(c). In the initial stages of evolution up to  $x \leq 6h$ , the  $k_z \phi_{\omega_z \omega_z}$  spectrum exhibits some activity in spanwise vortical motions, albeit not as pronounced as the  $k_z \phi_{\omega_y \omega_y}$  spectrum observed for the same streamwise positions. Beyond  $x = 6h$ , there is a noticeable recovery in the  $k_z \phi_{\omega_z \omega_z}$  spectrum, gradually aligning with the baseline provided by the PCH-DNS. At  $x = 24h$ , the energy represented by the  $k_z \phi_{\omega_z \omega_z}$  spectrum is consistent with the PCH-DNS across the entire range of scales.

Notably, the wall-normal vorticity's emergence underscores the pivotal role of the linear interaction between wall-normal velocity and vorticity in forming and sustaining the wall-layer streaks, as reported by Kim & Lim (2000). Additionally, the initial decay of the wall-normal velocity spectra during the spatial evolution of energy-containing motions, as detailed by Kannadasan *et al.* (2023), may be intricately connected to the excitation of

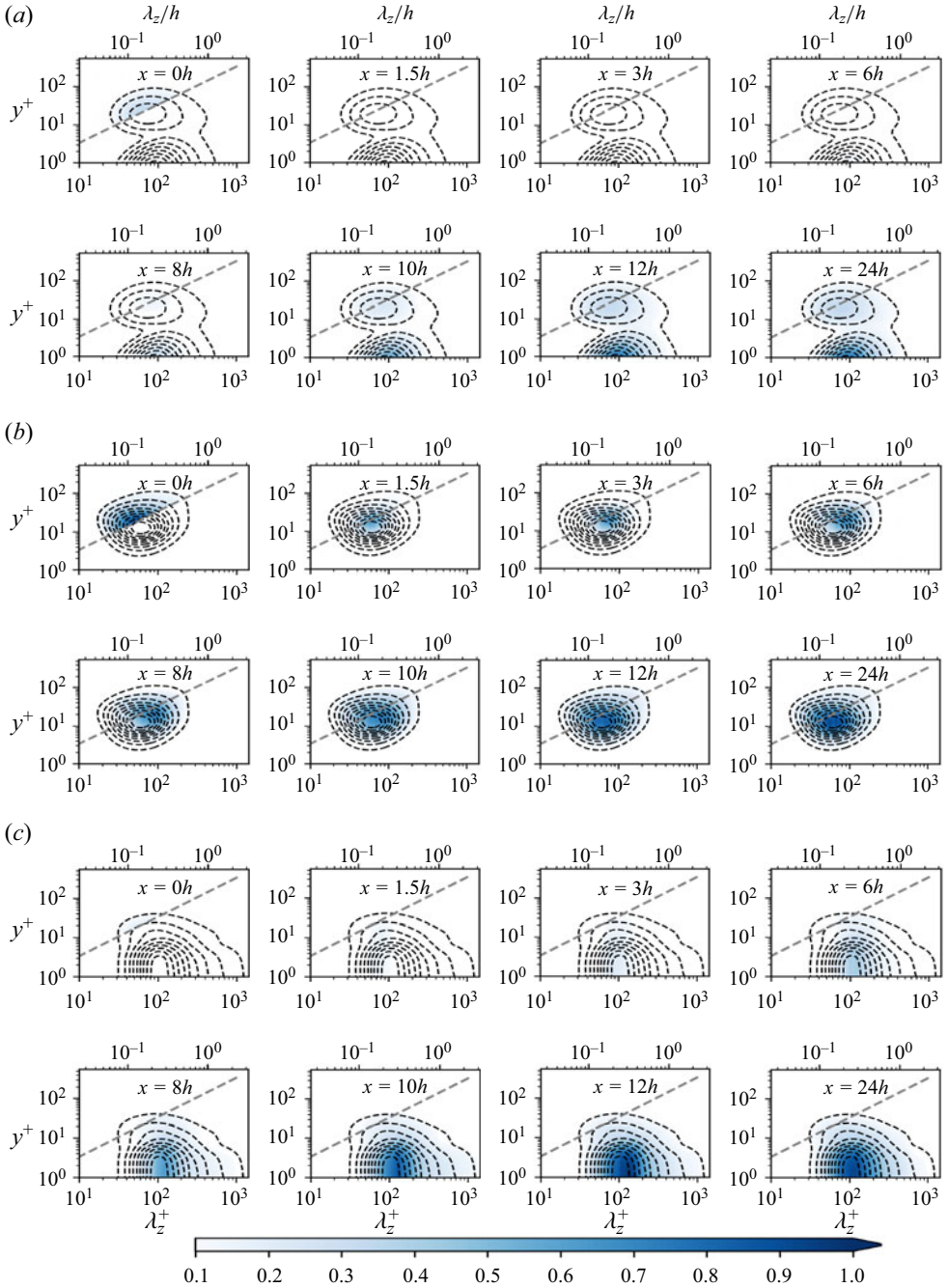


Figure 5. Premultiplied spanwise spectral distributions of (a) streamwise ( $k_z \phi_{\omega_x}$ ), (b) wall-normal ( $k_z \phi_{\omega_y}$ ) and (c) spanwise vorticity ( $k_z \phi_{\omega_z}$ ) shown with contours ranging from 0.1 to 1.0 of the maximum PCH-DNS value; PCH-DNS (black dashed line) and IOCH-DNS (coloured contours). The grey dashed line at  $\lambda_z = 3y$  denotes the cutoff wavelength.

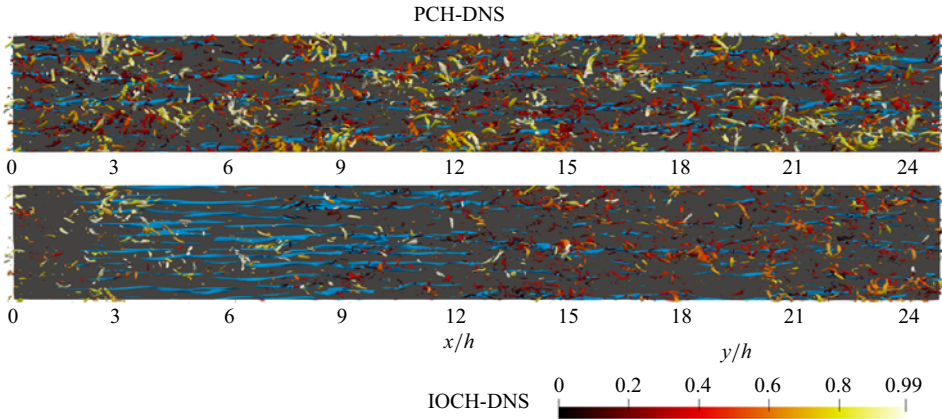


Figure 6. Vortices and low-speed structures visualised by the iso-surfaces of the second invariant of the velocity gradient tensor,  $Q_A/\langle Q_W \rangle = 3$ , the colour represents the distance from the wall, and the streamwise fluctuating velocity,  $u^+ = -0.5$  in blue, respectively. The invariant  $Q_A$  is normalised in terms of  $\langle Q_W \rangle$ , representing the mean value of second invariant of the rate-of-rotation tensor  $Q_W$ . The flow is from left to right.

wall-normal vorticity  $\omega_y$  via the linear coupling term  $\langle v'\omega'_y \rangle$ . Moreover, the findings of Jiménez & Pinelli (1999) indicate that the inhibition of the linear coupling term,  $\langle v'\omega'_z \rangle$ , can thwart the formation of streaky structures. Consequently, the linear coupling term is necessary for generating the wall-layer streaks (Kim & Lim 2000) and the instability of the formed streaks reinforces the streamwise vortices through a nonlinear process (Hamilton *et al.* 1995; Waleffe 1997).

The visual representation of low-speed structures, specifically streaks, and vortices within the synchronised DNS depicted in Figure 6, corroborates the findings from the velocity and vorticity spectra. It is evident from this visualisation that the energy-containing motions, which are a combination of the streaks and streamwise vortices, are removed from the neighbourhood of the inflow of the IOCH-DNS, and there is no evidence of the streaks or active vortical motions until  $x > 3h$ . The streaks start to re-appear beyond  $x = 3h$  and the vortical motions only start to become significant for  $x > 6h$ .

In summary, the spanwise velocity and vorticity spectra of the IOCH-DNS simulations have provided insights into the streamwise evolution of energy-containing motions and the formation of near-wall streaks. The recovery of energy-containing motions is shown to involve the formation of near-wall streaks and the wall-normal vorticity in the early stages of evolution. These observations of formation of near-wall streaks in the early stages of evolution and the decay of wall-normal and the spanwise velocity fluctuations are in line with typical transitions to turbulence, where the streaks are generated by extracting the energy from the mean flow and the wall-normal and spanwise velocity components decay while activating the long streaks in the flow (Landahl 1975; Butler & Farrell 1993). During this phase, the wall-normal and spanwise velocities tend to decay, which might actually activate the lift-up process of streaks through the linear coupling term, making them prominent in the spatial evolution of energy-containing motions. Furthermore, these findings are consistent with Jiménez & Pinelli (1999), who postulated that the removal of streaks leads to the adoption of secondary, albeit weaker, ‘bypass’ mechanisms for streak generation, suggesting that while advection by streamwise vortices predominantly facilitates streak creation, alternative mechanisms may take over in their absence.

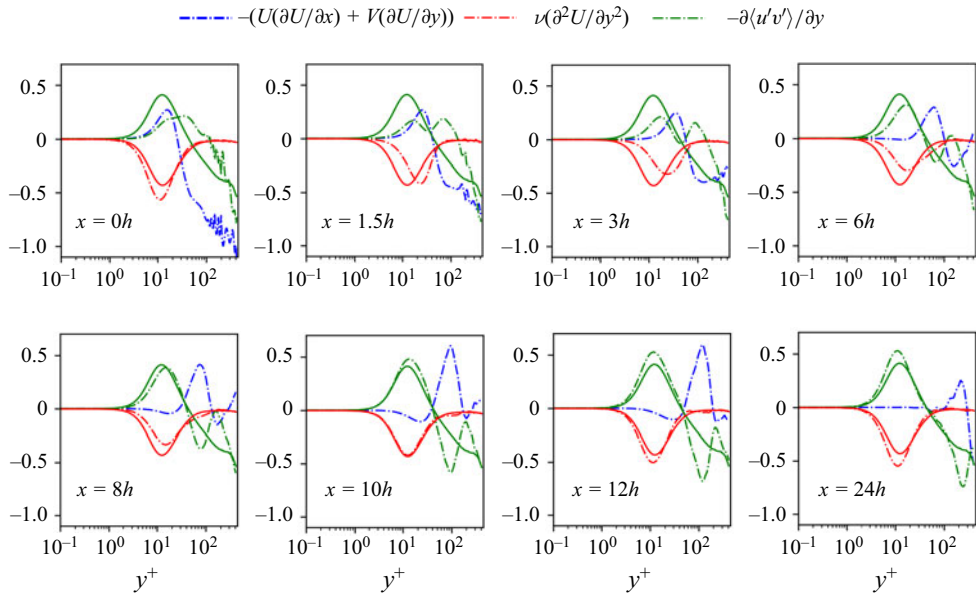


Figure 7. Spatial evolution of the streamwise momentum in the IOCH-DNS. Subpanels show the development of the streamwise momentum terms at increasing streamwise positions  $x/h$ : mean advection (blue), viscous stress gradient (red) and Reynolds shear stress gradient (green). The mean advection term is omitted for the PCH-DNS, as it represents a fully developed flow. Solid line, PCH-DNS; dash-dotted line, IOCH-DNS.

### 3.3. Mean momentum balance

The streamwise mean momentum equation for a spatially evolving IOCH-DNS is expressed as follows:

$$U \frac{\partial U}{\partial x} + V \frac{\partial U}{\partial y} = -\frac{1}{\rho} \frac{dP}{dx} + \nu \left( \frac{\partial^2 U}{\partial y^2} \right) - \frac{\partial \langle u'v' \rangle}{\partial y}. \quad (3.1)$$

The mean advection term is represented by the terms on the left-hand side of the (3.1). The terms on the right-hand side of (3.1) encompass the following: the mean pressure gradient that drives the flow,  $-(1/\rho)(dP/dx)$ , the gradient of the viscous stress,  $\nu(\partial^2 U/\partial y^2)$ , and the gradient of the Reynolds shear stress,  $\partial \langle u'v' \rangle/\partial y$ .

The spatial evolution of terms in the streamwise momentum equation (3.1), is presented in figure 7. The gradient of Reynolds shear stress,  $\partial \langle u'v' \rangle/\partial y$ , exhibits attenuation at  $x = 0h$ , as a result of filtering the energy-containing motions at the IOCH-DNS inflow. The mean advection at the inflow ( $x = 0h$ ) shows a significant change in the mean velocity field resulting from streamwise advection, represented by  $U\partial U/\partial x$ .

As the flow advances, the gradient of viscous stress diminishes, while the Reynolds stress gradient begins to develop within the buffer layer, specifically for  $y^+ \approx 10 \simeq 20$ , during the early evolution stages at  $x = 1.5h \simeq 6h$ , as indicated in figure 7. Beyond  $x = 6h$ , the gradient of viscous stress starts to recover, aligning with the fully developed PCH-DNS at  $x = 10h$ . Concurrently, the Reynolds stress gradient quickly regains its strength in the buffer layer, matching the PCH-DNS at  $x = 10h$ . For  $x \geq 8h$ , both the viscous stress gradient and the Reynolds shear stress gradient are balanced, which is a commonly observed characteristic in the near-wall region of a fully developed channel flow.

### Interplay of scales of energy-containing motions

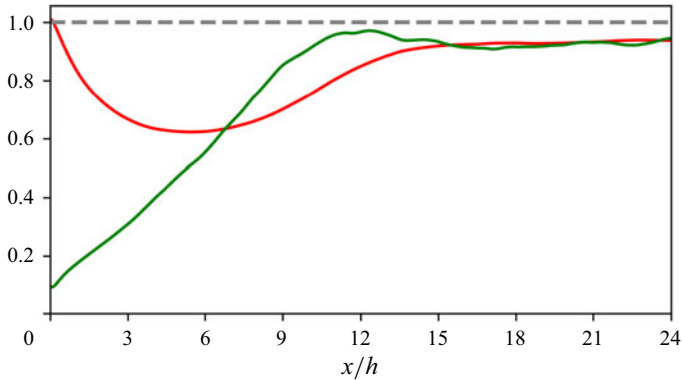


Figure 8. Ratio of the mean kinetic energy (MKE) and turbulent kinetic energy (TKE) between the IOCH-DNS and PCH-DNS, integrated for  $y^+ \leq 30$ . Red line,  $MKE_{IOCH-DNS}/MKE_{PCH-DNS}$ ; green line,  $TKE_{IOCH-DNS}/TKE_{PCH-DNS}$ .

Kannadasan *et al.* (2023) observed that the mean flow velocity profile in the IOCH-DNS decays in the near-wall region during the initial stages of evolution,  $x \leq 6h$ , and then gradually recovers to its fully developed state. During the early stages,  $x \leq 6h$ , the mean advection term exhibits a predominantly negative value within the log-layer. This implies that the mean flow is actively transporting momentum towards the wall, resulting in a reduction of the mean flow velocity within the near-wall region. This decaying trend in the mean velocity profile is further associated with the evolution of the Reynolds shear stress gradient in the near-wall region during this phase, as shown in figure 7.

Figure 8 shows the distribution of both mean kinetic energy (MKE) and TKE, which have been integrated in the wall-normal direction for  $y^+ \leq 30$  – a region where the mean velocity profile undergoes noticeable changes, as reported by Kannadasan *et al.* (2023). Figure 8 shows a reduction in MKE along the streamwise direction with the observed recovery of TKE for  $x \leq 6h$ . These results align with the observations made regarding the mean advection and Reynolds stress gradient profiles illustrated in figure 7. Consequently, it can be inferred that the distortion of the mean velocity profile and the evolution of TKE within the buffer layer are indicative of the transfer of energy from the mean flow, primarily facilitated by mean advection, to generate TKE.

For  $x > 6h$ , the mean advection term in the near-wall region ( $y^+ < 30$ ) approaches zero, signifying the attainment of a fully developed state, as the Reynolds stress gradient is completely recovered in this region. In contrast, in the log-layer, the mean advection becomes predominantly positive, facilitating momentum transfer away from the wall and indicating TKE production. For  $x \geq 8h$ , in the log-layer,  $y^+ \approx 80 \simeq 150$ , the mean advection term and the gradient of the Reynolds shear stress are almost balanced, signifying TKE production in the log-layer, driven by the Reynolds shear stress through mean advection.

In summary, the mean advection term is instrumental in the early decay and subsequent recovery of the mean velocity profile, as well as the restoration of the Reynolds stress gradient in the near-wall region, by facilitating momentum transfer towards the wall. Once the Reynolds stress gradient profile in the near-wall region reaches a fully developed state (for  $x > 6h$ ), the mean advection term nears zero, signifying its role in the recovery of Reynolds stress and consequently in the generation of TKE in the near-wall region.

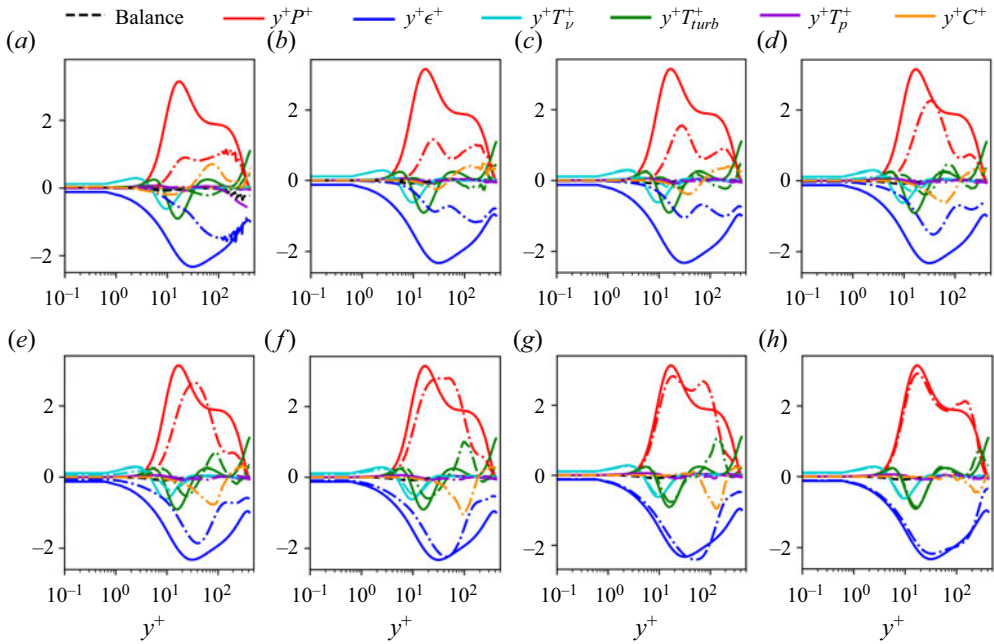


Figure 9. Turbulent kinetic energy budget of the IOCH-DNS as a function of  $y$  at various streamwise locations: (a)  $x = 0h$ ; (b)  $x = 1.5h$ ; (c)  $x = 3h$ ; (d)  $x = 6h$ ; (e)  $x = 8h$ ; (f)  $x = 10h$ ; (g)  $x = 12h$  and (h)  $x = 24h$ . Solid line, PCH-DNS; dash-dotted line, IOCH-DNS.

### 3.4. Wall-normal distributions of TKE budget in the IOCH-DNS

To examine the energy transfer mechanisms in the spatial development of energy-containing motions in the IOCH-DNS, the TKE budget in (2.1) is analysed. A comparison of TKE production ( $y^+P^+$ ) and dissipation ( $y^+\epsilon^+$ ) profiles in the IOCH-DNS and PCH-DNS is shown in figure 9. In the IOCH-DNS, production and dissipation profiles largely remain constant across the wall-normal distance, except for the buffer layer for  $x \leq 6h$ . With the flow development, TKE production and dissipation intensify in the buffer layer, whereas transport terms are not significant for  $x \leq 6h$ . The increase in TKE production in the buffer layer up to  $x \leq 6h$  correlates with near-wall streak formation, as evidenced by the amplified one-dimensional streamwise velocity spectra in IOCH-DNS relative to PCH-DNS in early stages. Following TKE re-establishment in the buffer layer, turbulent production in the log-layer strengthens, as shown in figure 9(g) at  $x = 12h$ . There is also a significant energy transfer through the turbulent transport term in the log-layer for  $x > 6h$ .

The mean advection term is initially positive in the log-layer during early-stage evolution of energy-containing motions in the IOCH-DNS  $x \leq 6h$ , indicative of TKE being transported towards the wall. As the flow develops, the mean convection term in the near-wall region ( $y^+ \leq 30$ ) approaches zero, indicating that the flow progresses towards a fully developed state in this region by  $x \geq 12h$ , as shown in figure 9(g,h). In the log-layer, mean convection nearly balances with the turbulent transport and excessive production for  $x = 8h \simeq 12h$ , as shown in figure 9(e,f,g), indicating the redistribution of energy from the mean flow through the turbulent transport term.

In summary, the production of TKE near the wall accelerates more rapidly than in the logarithmic layer. Following the re-establishment of TKE in the buffer layer, there is an increase in TKE production within the logarithmic layer. The observed balance between mean convection and turbulent transport, accompanied by increased production, suggests that TKE may be locally generated in the logarithmic layer or transported in the wall-normal direction or across scales through the turbulent transport term. These processes will be further explored in the sections on spectral analysis of TKE production in § 3.6 and interscale transport of TKE in § 3.8.

### 3.5. Wall-normal distributions of Reynolds stress budget in the IOCH-DNS

The streamwise Reynolds stress budget for the IOCH-DNS, normalised using wall units, is presented in figure 10. Downstream evolution of the flow is marked by a significant increase in both production and dissipation of streamwise Reynolds stresses within the buffer layer, as depicted in figure 10(a). Concurrently, the streamwise pressure-strain redistribution term exhibits a decrease for  $x \leq 6h$ , as illustrated in figure 10(b), indicating a reduced redistribution of energy from  $\langle u'^2 \rangle$  to  $\langle v'^2 \rangle$  and  $\langle w'^2 \rangle$ . Furthermore, the turbulent transport term is observed to actively transfer energy both towards and away from the wall for  $x \geq 6h$ , as shown in figure 10(b), with the peak of the turbulent production term approaching the levels seen in the fully developed PCH-DNS. Beyond  $x > 6h$ , the streamwise pressure-strain term begins to rise from its initial decrease, eventually surpassing the values of the fully developed PCH-DNS in the logarithmic layer for  $x \geq 12h$ , as depicted in figure 10(b).

The wall-normal Reynolds stress budget for the IOCH-DNS, normalised by wall units, is depicted in figure 11. As the flow progresses streamwise within the IOCH-DNS, the wall-normal pressure-strain term  $\Pi_y^+$ , a source term for  $v'^2$ , exhibits a streamwise decay, accompanied by a decrease in wall-normal Reynolds stress dissipation for  $x \leq 6h$ . Notably, post  $x = 6h$ , a region where streaks are re-established, the wall-normal pressure-strain term begins to recover in the buffer layer, indicating a redistribution of energy to wall-normal fluctuations from the streamwise fluctuations. This recovery of the wall-normal pressure-strain term beyond  $x = 6h$  aligns with the recovery of wall-normal fluctuations  $v'^2$ , consistent with velocity spectra observations by Kannadasan *et al.* (2023), where an initial decay in the  $v'^2$  spectrum is followed by a recovery as the near-wall energy of the  $u'^2$  spectrum is reinstated at the wavelength of streak spacing. During this phase, the turbulent transport term remains relatively insignificant until the wall-normal pressure strain term recovers, as shown in figure 11(b–d).

The pressure-strain term  $\Pi_z^+$  of the the spanwise Reynolds stress budget remains unchanged for  $x \leq 6h$ , as shown in figure 12. This stability in the  $\Pi_z^+$  term aligns with the spanwise velocity spectra observations of Kannadasan *et al.* (2023), where spanwise velocity fluctuations remain constant for  $x \leq 6h$ . Beyond  $x = 6h$ , the  $\Pi_z^+$  term shows a recovery, surpassing the levels observed in the PCH-DNS at  $x = 12h$ , indicating an increased redistribution of energy to  $w'^2$ . The role of the convective term in this process is significant, particularly in facilitating the recovery of the  $\Pi_z^+$  term, as shown in figure 12(e–g).

In summary, the investigation of streamwise, wall-normal and spanwise Reynolds stress budgets in the IOCH-DNS exhibits distinct patterns in the pressure-strain terms  $\Pi_x^+$ ,  $\Pi_y^+$  and  $\Pi_z^+$ , which exhibit strong correlations with the velocity spectra. Specifically, the increased production of streamwise Reynolds stress and the decline of the  $\Pi_x^+$  term correspond with the recovery of streamwise velocity fluctuations, as discussed in § 3.1.

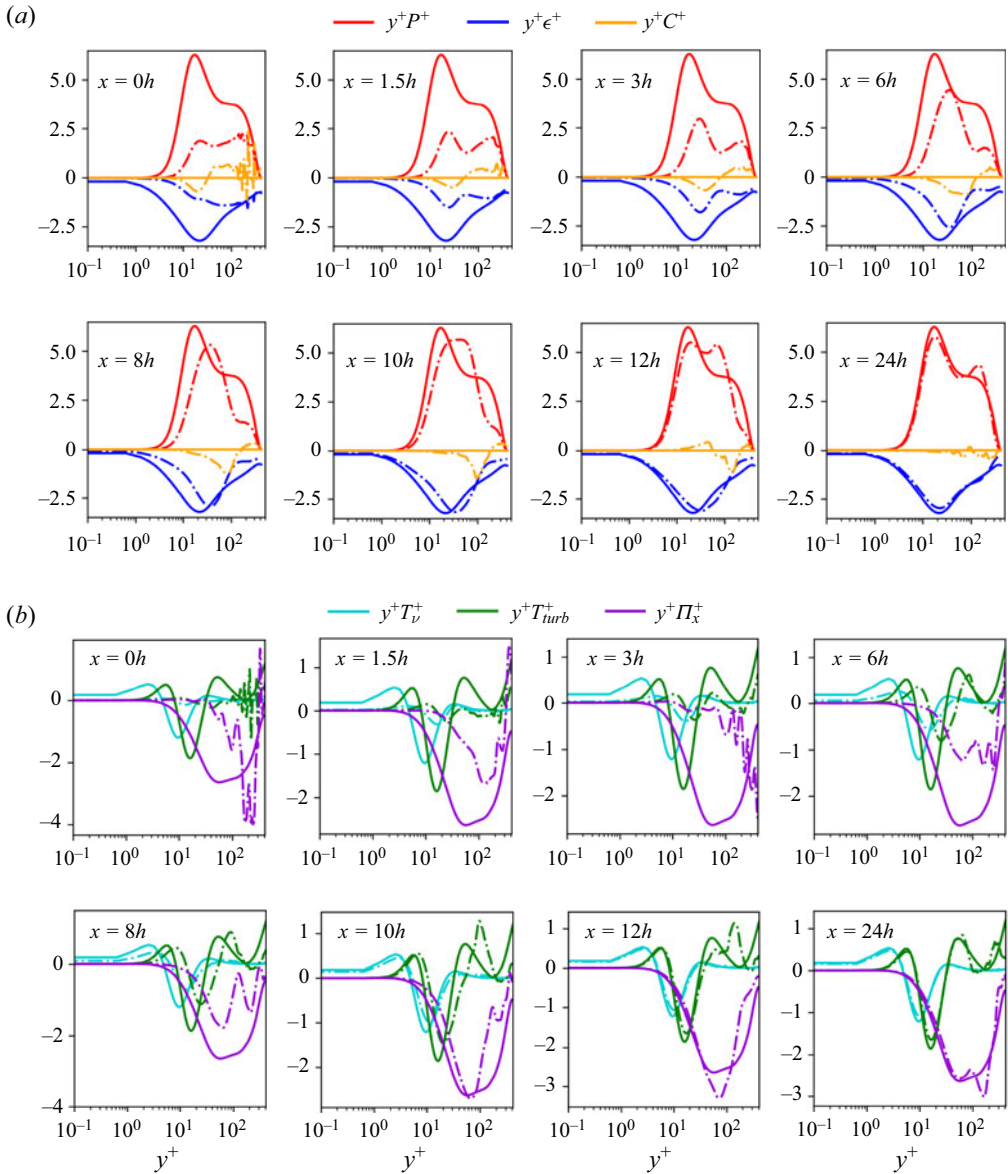


Figure 10. Streamwise Reynolds stress budget of the IOCH-DNS as a function of  $y$  at various streamwise locations: (a) production, dissipation and convection terms; (b) turbulent transport, pressure-strain and viscous transport terms. Solid line, PCH-DNS; dash-dotted line, IOCH-DNS.

Concurrently, the  $\Pi_y^+$  term initially decreases and then recovers, mirroring the early-stage decay of wall-normal velocity fluctuations reported by Kannadasan *et al.* (2023). In contrast, the spanwise pressure-strain term  $\Pi_z^+$  remains constant initially and then rises, reflecting the stable spanwise velocity fluctuations until  $x \leq 6h$  and their subsequent recovery. Therefore, the minimal pressure-strain redistribution is linked to the decline of wall-normal velocity fluctuations and the persistence of spanwise velocity fluctuations in the early stages of flow evolution in the IOCH-DNS. Further insights, including an analysis of the pressure-strain spectrum, are discussed in § 3.7.

Interplay of scales of energy-containing motions

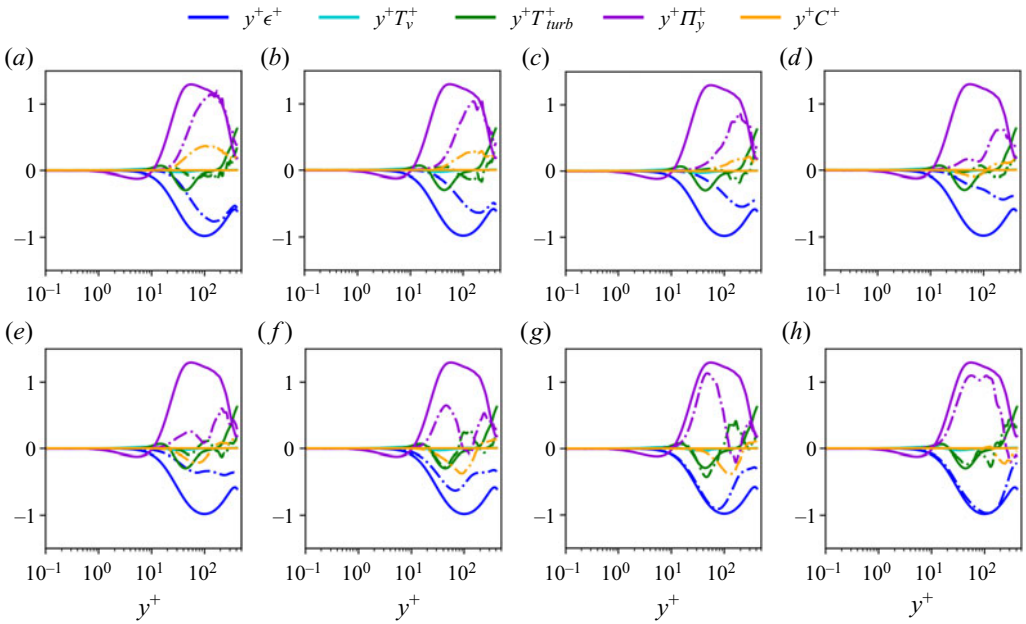


Figure 11. Wall-normal Reynolds stress budget of the IOCH-DNS as a function of  $y$  at various streamwise locations: (a)  $x = 0h$ ; (b)  $x = 1.5h$ ; (c)  $x = 3h$ ; (d)  $x = 6h$ ; (e)  $x = 8h$ ; (f)  $x = 10h$ ; (g)  $x = 12h$  and (h)  $x = 24h$ . Solid line, PCH-DNS; dash-dotted line, IOCH-DNS.

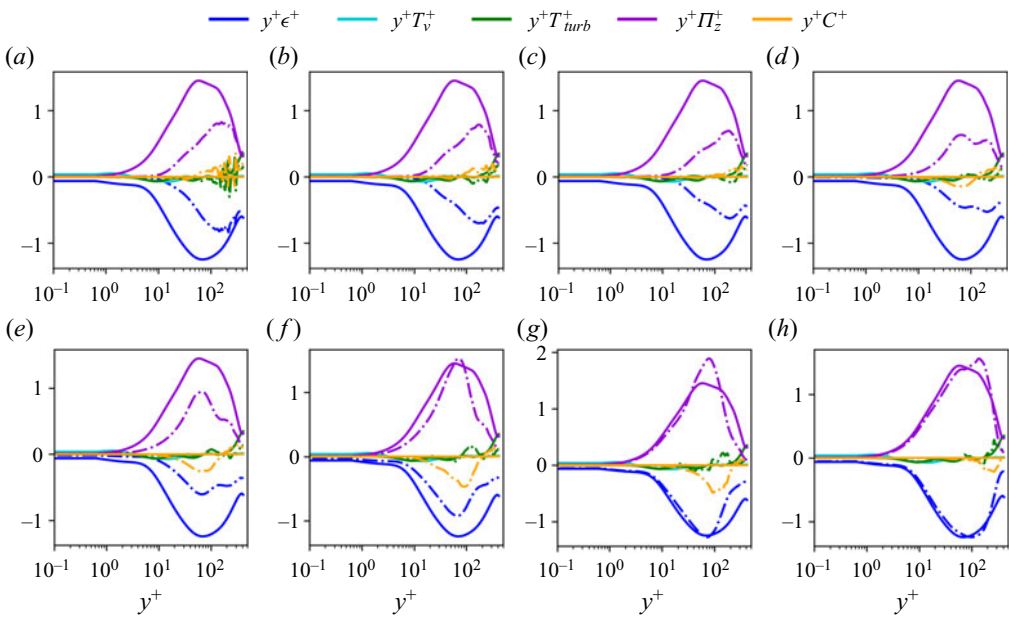


Figure 12. Spanwise Reynolds stress budget of the IOCH-DNS as a function of  $y$  at various streamwise locations: (a)  $x = 0h$ ; (b)  $x = 1.5h$ ; (c)  $x = 3h$ ; (d)  $x = 6h$ ; (e)  $x = 8h$ ; (f)  $x = 10h$ ; (g)  $x = 12h$  and (h)  $x = 24h$ . Solid line, PCH-DNS; dash-dotted line, IOCH-DNS.

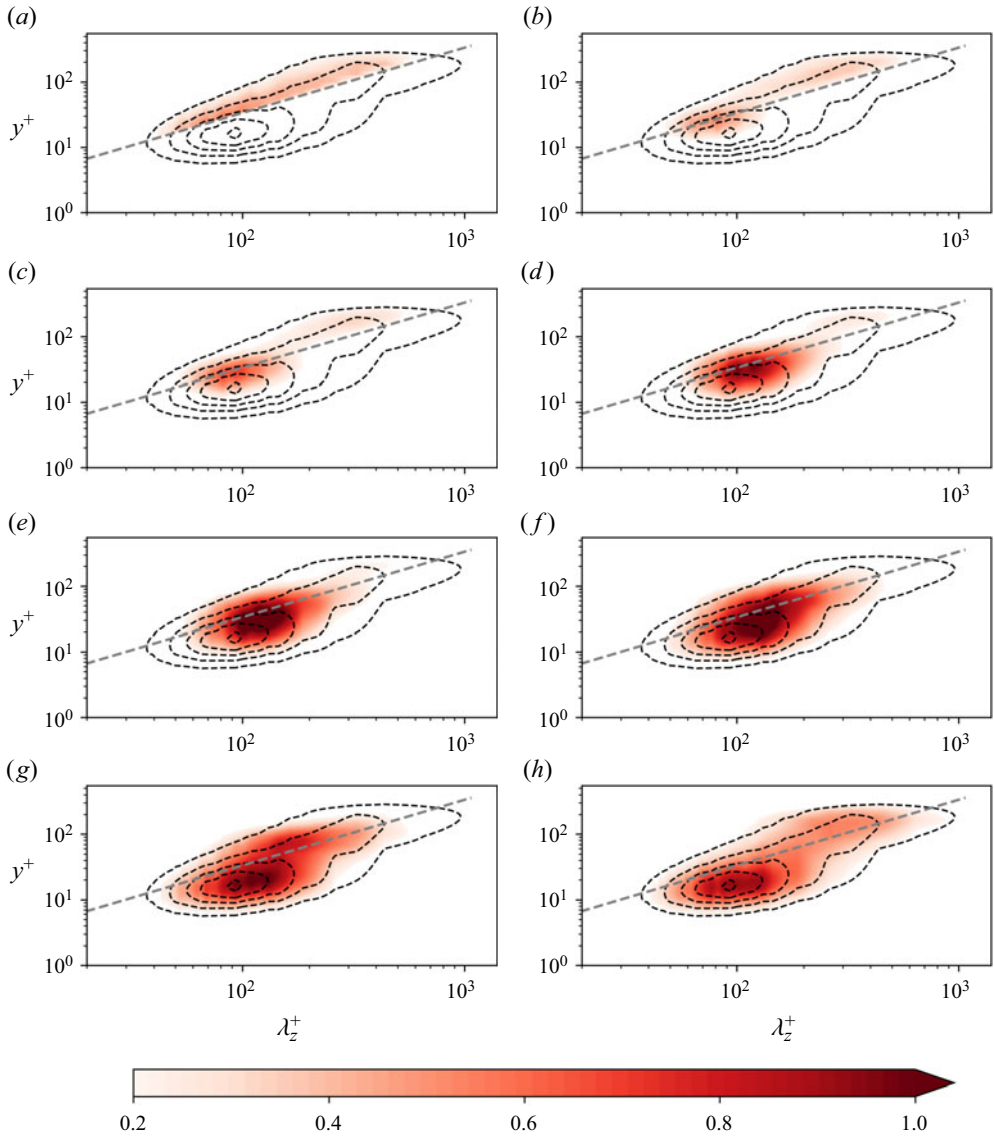


Figure 13. Premultiplied spanwise wavenumber spectra of TKE production  $k_z y^+ \widehat{P}^+$  as a function of  $y$  at various streamwise locations: (a)  $x = 0h$ ; (b)  $x = 1.5h$ ; (c)  $x = 3h$ ; (d)  $x = 6h$ ; (e)  $x = 8h$ ; (f)  $x = 10h$ ; (g)  $x = 12h$ ; (h)  $x = 24h$ . The dashed black line represents the PCH-DNS data, with contour levels shown as  $[0.2, 0.4, 0.6, 0.8, 1]$ . The red contours depict the IOCH-DNS data. Here, the grey dashed line is at  $\lambda_z = 3y$  to indicate the cutoff spanwise wavelength.

### 3.6. Spectral analysis of turbulent kinetic energy production

Figure 13 illustrates the spatial evolution of premultiplied spanwise spectra of TKE production ( $k_z^+ y^+ \widehat{P}^+$ ) along the streamwise direction in the ICOH-DNS. In the PCH-DNS case, the TKE production spectra peak occurs at  $\lambda_z^+ \simeq 100$  and  $y^+ \simeq 15$ , as indicated by the dashed black lines in figure 13.

### *Interplay of scales of energy-containing motions*

In the IOCH-DNS case, as the flow develops, the  $k_z^+ y^+ \widehat{P}^+$  spectrum gets stronger around a spanwise wavelength equivalent to the near-wall spacing of streaks,  $\lambda_z^+ \simeq 100$ , as shown in [figure 13\(b–d\)](#). This indicates the formation of near-wall streaks at the early stage of streamwise evolution of energy-containing motions, consistent with the findings of velocity spectra in §3.1. Additionally, the amplitude of the  $k_z^+ y^+ \widehat{P}^+$  spectrum at the near-wall streak location,  $\lambda_z^+ \simeq 100$ , for  $6h \leq x \leq 10h$  is higher in the IOCH-DNS case compared with the PCH-DNS case. This suggests that the streaks are significantly amplified in the recovery of energy-containing motions, ultimately leading to the breakdown of the streaks and the initiation of the self-sustaining process.

The spectral density of TKE production above the ridge exhibits a streamwise decrease for  $x \leq 6h$ , as depicted in [figure 13\(b–d\)](#). During this phase, the predominant factor is the recovery of streamwise energy at the streak location, accompanied by the decay of wall-normal and spanwise energy. This process is integral to activating near-wall streaks in the flow, resulting in an overall reduction of TKE above the ridge. Beyond  $x > 12h$ , the  $k_z^+ y^+ \widehat{P}^+$  spectrum above the ridge in the IOCH-DNS aligns with the corresponding PCH-DNS case ([figure 13h](#)). This alignment suggests that TKE production in the motions responsible for energy cascading occurs once the near-wall streaks are reformed. Furthermore, it implies that TKE is either transported in the wall-normal direction or transformed across scales, rather than being locally generated within the energy-cascading motions.

#### *3.7. Inter-component energy transfer*

The pressure-strain correlation plays a significant role in redistributing the TKE from  $\langle u'^2 \rangle$  to the other two velocity components,  $\langle v'^2 \rangle$  and  $\langle w'^2 \rangle$ , as the TKE production only occurs in the  $\langle u'^2 \rangle$  component, while the pressure-strain term acts as a source for  $\langle v'^2 \rangle$  and  $\langle w'^2 \rangle$ . The pressure-strain correlations in the RSTE (2.7) can be expressed in Fourier space as

$$\widehat{\Pi}_x(y, k_z) = \left\langle \text{Re} \left\{ \widehat{p}' \frac{\partial \widehat{u}^{*'}}{\partial x} \right\} \right\rangle, \quad (3.2a)$$

$$\widehat{\Pi}_y(y, k_z) = \left\langle \text{Re} \left\{ \widehat{p}' \frac{\partial \widehat{v}^{*'}}{\partial y} \right\} \right\rangle, \quad (3.2b)$$

$$\widehat{\Pi}_z(y, k_z) = \left\langle \text{Re} \left\{ \widehat{p}' \frac{\partial \widehat{w}^{*'}}{\partial z} \right\} \right\rangle. \quad (3.2c)$$

The pressure-strain terms given in (3.2c) do not appear in the spectral TKE budget equation (2.3) since the continuity equation leads to

$$\widehat{\Pi}_x(y, k_z) + \widehat{\Pi}_y(y, k_z) + \widehat{\Pi}_z(y, k_z) = 0, \quad (3.3)$$

where  $\widehat{\Pi}_x(y, k_z)$ ,  $\widehat{\Pi}_y(y, k_z)$  and  $\widehat{\Pi}_z(y, k_z)$  are the spanwise wavenumber spectra of the streamwise, wall-normal and spanwise components of pressure-strain terms, respectively.

[Figure 14](#) illustrates the premultiplied spanwise spectra of the streamwise pressure-strain component ( $\widehat{\Pi}_x(y, k_z)$ ) and its streamwise development. The PCH-DNS  $\widehat{\Pi}_x(y, k_z)$  spectrum is represented as dashed lines and is observed to be negative due to the transfer of TKE from  $\langle u'^2 \rangle$  to  $\langle v'^2 \rangle$  and  $\langle w'^2 \rangle$  by the streamwise pressure-strain component.

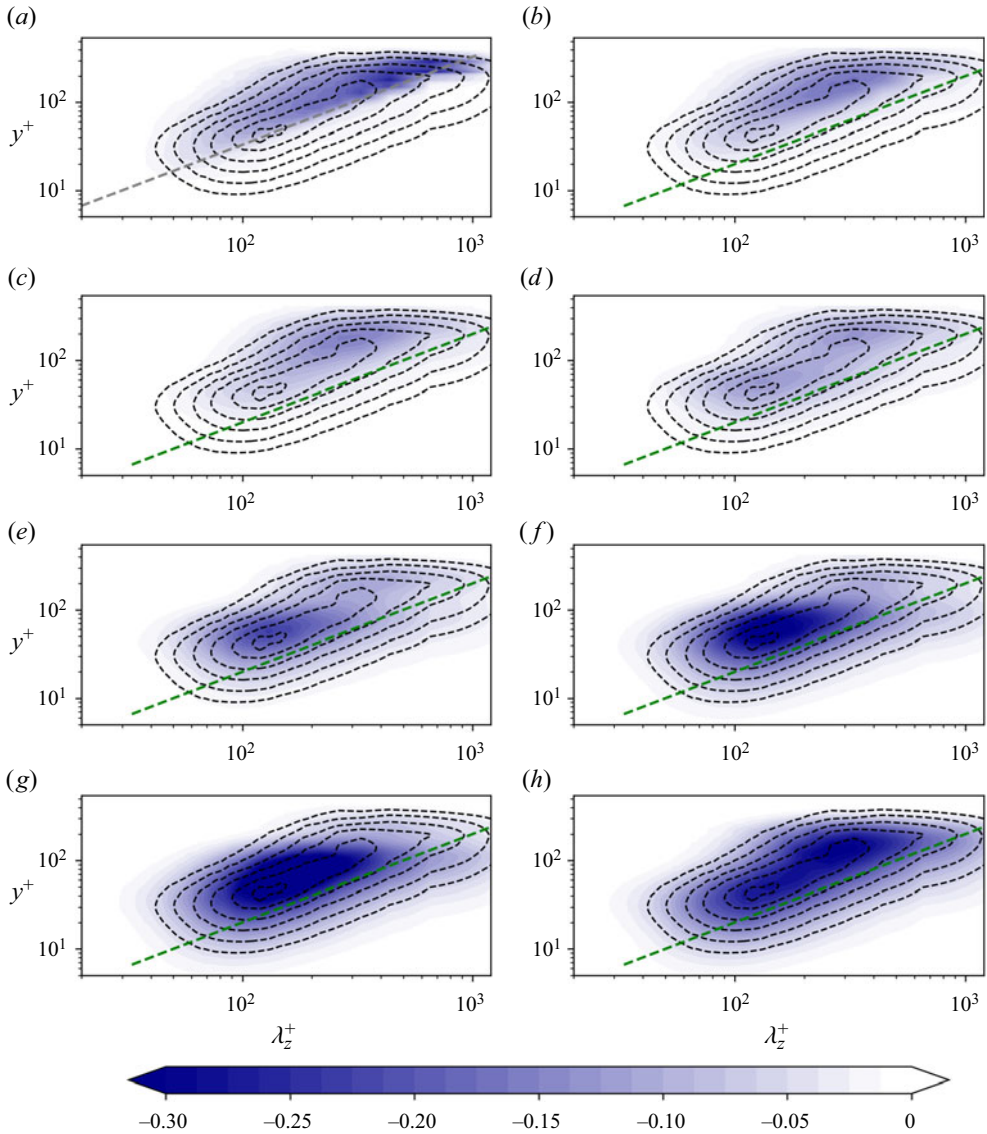


Figure 14. Premultiplied spanwise wavenumber spectra of streamwise pressure-strain  $k_z^+ y^+ \hat{\Pi}_x^+$  as a function of  $y$  at various streamwise locations: (a)  $x = 0h$ ; (b)  $x = 1.5h$ ; (c)  $x = 3h$ ; (d)  $x = 6h$ ; (e)  $x = 8h$ ; (f)  $x = 10h$ ; (g)  $x = 12h$ ; (h)  $x = 24h$ . The dashed black line represents the PCH-DNS data, with contour levels shown as  $[-0.3, -0.25, -0.2, -0.15, -0.1, -0.05]$ . The blue contours depict the IOCH-DNS data. Here, the grey dashed line in panel (a) is at  $\lambda_z = 3y$  to indicate the cutoff spanwise wavelength and the green dashed line in panels (b)–(h) is at  $\lambda_z = 5y$ .

Additionally, the alignment of the  $\hat{\Pi}_x(y, k_z)$  spectrum along  $\lambda_z = 5y$  in the PCH-DNS confirms the energy redistribution at an integral length scale, consistent with previous studies (Cho *et al.* 2018; Lee & Moser 2019).

The IOCH-DNS data reveal an interesting behaviour characterised by an insignificant streamwise pressure-strain component for  $x \leq 6h$ , consistent with the streamwise Reynolds stress budget discussed in §3.5. This observation suggests a negligible

inter-component redistribution of TKE from  $\langle u'^2 \rangle$  to  $\langle v'^2 \rangle$  and  $\langle w'^2 \rangle$  in this region, despite the significant production of TKE as discussed in §3.6. The concurrent presence of substantial TKE production and the lack of significant redistribution of streamwise energy to  $\langle v'^2 \rangle$  and  $\langle w'^2 \rangle$  for  $x \leq 6h$  aligns with the observations of the wall-normal and spanwise velocity spectra of the IOCH-DNS reported by Kannadasan *et al.* (2023), where the wall-normal and spanwise velocity spectra exhibit a decay in energy, while the streamwise velocity spectra display a recovery trend.

The absence of active streamwise vorticity for  $x \leq 6h$  can be attributed to the inactive pressure-strain redistribution within this interval. The limited effective redistribution of streamwise energy to the wall-normal and spanwise components, coupled with the predominant use of MKE for streak production, collectively results in the absence of active vortical motions for  $x \leq 6h$ . Essentially, this region represents a phase where streamwise vortices have not yet fully recovered, and the primary process at play involves the formation of near-wall streaks.

Figure 15 presents a comparison of the premultiplied spanwise spectra of the wall-normal pressure-strain,  $k_z \widehat{\Pi}_y(y, k_z)$ , for the PCH-DNS and IOCH-DNS. In the PCH-DNS, the  $k_z \widehat{\Pi}_y(y, k_z)$  is expected to exhibit a close alignment along the linear ridge  $\lambda_z = 5y$ , similar to the  $k_z \widehat{\Pi}_x(y, k_z)$  spectrum. This alignment arises from the fact that all the pressure-strain terms in (3.2c) are solely functions of the spanwise wavenumber,  $k_z$ , and they should satisfy the condition outlined in (3.3). Additionally, the  $k_z \widehat{\Pi}_y(y, k_z)$  spectra are predominantly positive, indicative of energy gain from the streamwise velocity component.

However, the  $k_z \widehat{\Pi}_y(y, k_z)$  spectra of the PCH-DNS also exhibits a weak negative region at  $y^+ \simeq 5$ , representing the well-known Splat effect that causes energy transfer from the wall-normal  $\langle v'^2 \rangle$  to spanwise  $\langle w'^2 \rangle$  velocity fluctuations. In contrast, the IOCH-DNS shows negligible energy re-distribution to  $\langle v'^2 \rangle$  from  $\langle u'^2 \rangle$  until  $x = 6h$ , and no transfer of energy from  $\langle v'^2 \rangle$  to  $\langle w'^2 \rangle$  for  $x \leq 6h$  in the near-wall region. The absence of energy transfer from  $\langle v'^2 \rangle$  to  $\langle w'^2 \rangle$  in the early stages of evolution in the IOCH-DNS is likely due to the lack of splat effect by the fluid moving towards the wall, which inhibits the transfer of energy from the wall-normal to the spanwise velocity component.

Figure 16 illustrates a comparison between the spanwise spectra of the spanwise pressure-strain,  $k_z \widehat{\Pi}_z(y, k_z)$ , for the PCH-DNS and IOCH-DNS. The PCH-DNS spectrum aligns along the ridge  $\lambda_z = 5y$ , consistent with the relationship presented in (3.3). The behaviour of the spanwise pressure-strain spectra ( $k_z \widehat{\Pi}_z(y, k_z)$ ) in the IOCH-DNS follows a pattern akin to that observed in the wall-normal pressure-strain spectra. Specifically, it exhibits a noteworthy characteristic: there is an absence of significant pressure-strain redistribution of energy from the streamwise component to the spanwise component for  $x < 6h$ , and this redistribution mechanism becomes active only after reaching  $x = 6h$ , coinciding with the region where the streaks are re-established.

The analysis of pressure-strain correlations in the IOCH-DNS highlights a notable association between the inter-component TKE transfer and the generation of small-scale vortices through streak breakdown. This connection becomes evident when considering the insignificant pressure-strain redistribution for  $x < 6h$ . During this phase, the streamwise vortical motions remain inactive. It is crucial to emphasise that the lack of active vortical motions for  $x < 6h$  stems from the inactivity of pressure-strain redistribution within that region. In particular, it is observed that the streamwise vortices commence their evolution at smaller length scales ( $\lambda_z^+ \leq 200$ ) at  $x = 8h$ , which coincides with the streamwise position where the pressure-strain redistribution reactivates. Thus, the observed behaviour underscores the pivotal role of streak formation as the

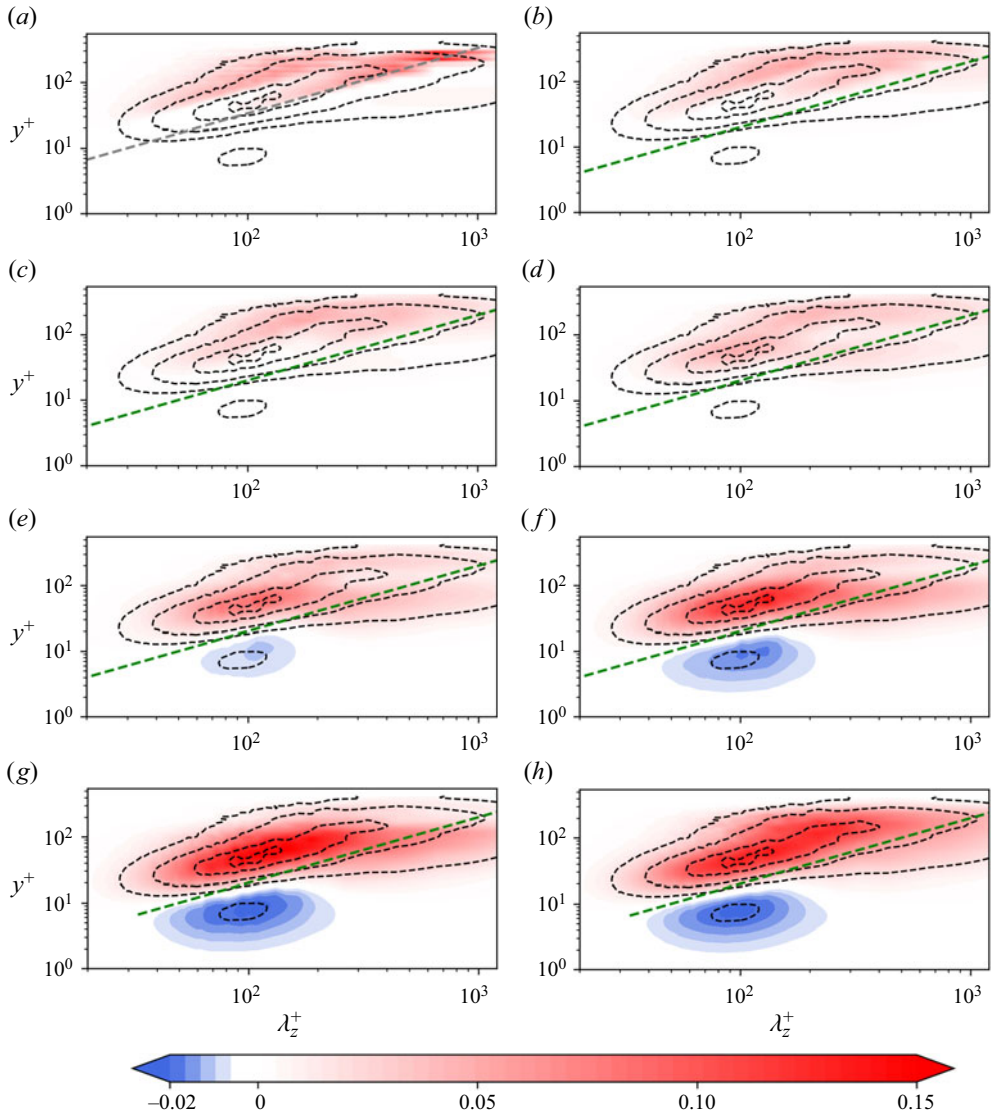


Figure 15. Premultiplied spanwise wavenumber spectra of wall-normal pressure-strain  $k_z^+ y^+ \hat{\Pi}_y^+$  as a function of  $y$  at various streamwise locations: (a)  $x = 0h$ ; (b)  $x = 1.5h$ ; (c)  $x = 3h$ ; (d)  $x = 6h$ ; (e)  $x = 8h$ ; (f)  $x = 10h$ ; (g)  $x = 12h$ ; (h)  $x = 24h$ . The dashed black line represents the PCH-DNS data, with contour levels shown as  $[-0.02, 0.025, 0.05, 0.1, 0.15]$ . The coloured contours depict the IOCH-DNS data. Here, the grey dashed line is at  $\lambda_z = 3y$  to indicate the cutoff spanwise wavelength and the green dashed line is at  $\lambda_z = 5y$ .

dominant process in the  $x < 6h$  region, with the subsequent reactivation of pressure-strain redistribution and the formation of streamwise vortices.

### 3.8. Interscale transport of TKE

Figure 17 shows the interscale transport of TKE ( $k_z y^+ t_{r_{kt}}$ ) based on (2.12c) and (2.13), which exhibits both positive and negative regions. The negative isocontour indicates local energy loss at a particular scale, while the positive isocontour signifies energy

Interplay of scales of energy-containing motions

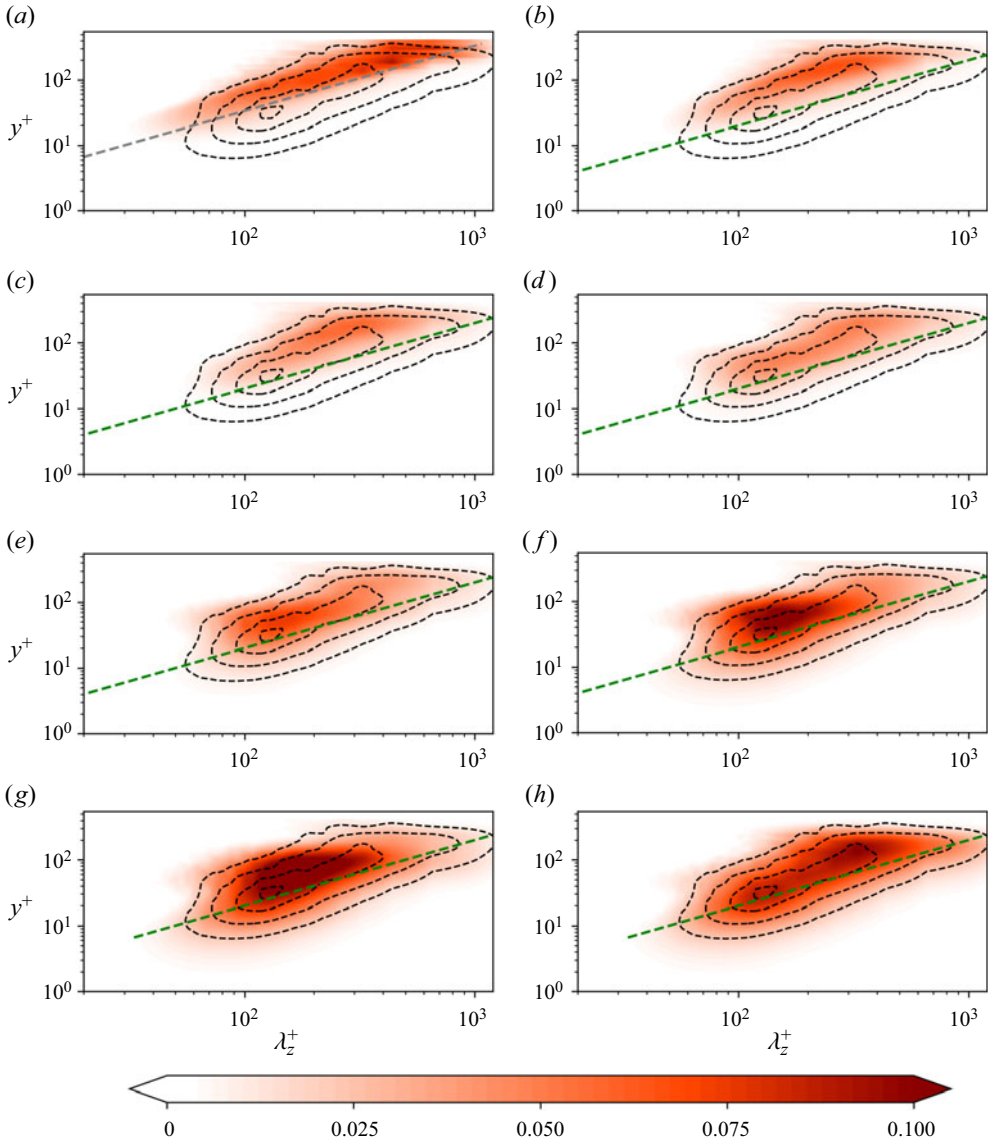


Figure 16. Premultiplied spanwise wavenumber spectra of spanwise pressure-strain  $k_z^+ y^+ \hat{\Pi}_z^+$  as a function of  $y$  at various streamwise locations: (a)  $x = 0h$ ; (b)  $x = 1.5h$ ; (c)  $x = 3h$ ; (d)  $x = 6h$ ; (e)  $x = 8h$ ; (f)  $x = 10h$ ; (g)  $x = 12h$ ; (h)  $x = 24h$ . The dashed black line represents the PCH-DNS data, with contour levels shown as  $[0.025, 0.05, 0.075, 0.1]$ . The red contours depict the IOCH-DNS data. Here, the grey dashed line is at  $\lambda_z = 3y$  to indicate the cutoff spanwise wavelength and the green dashed line is at  $\lambda_z = 5y$ .

gain at a given scale due to interscale flux  $T_{rij}^{kt}$ . In the PCH-DNS, the negative region aligns well along the ridge  $\lambda_z = 5y$ , which corresponds to the TKE production spectrum. Notably, there are two positive regions in the PCH-DNS: one is situated to the left of the negative region at a spanwise wavelength of  $\lambda_z^+ \simeq 30$ , representing the forward energy cascade from large to small scales, while the second positive region is positioned to the right of the negative region at a wavelength  $\lambda_z^+ \simeq 300$ , indicating the inverse energy cascade from small to large scales. The near-wall peak of the negative region lies at

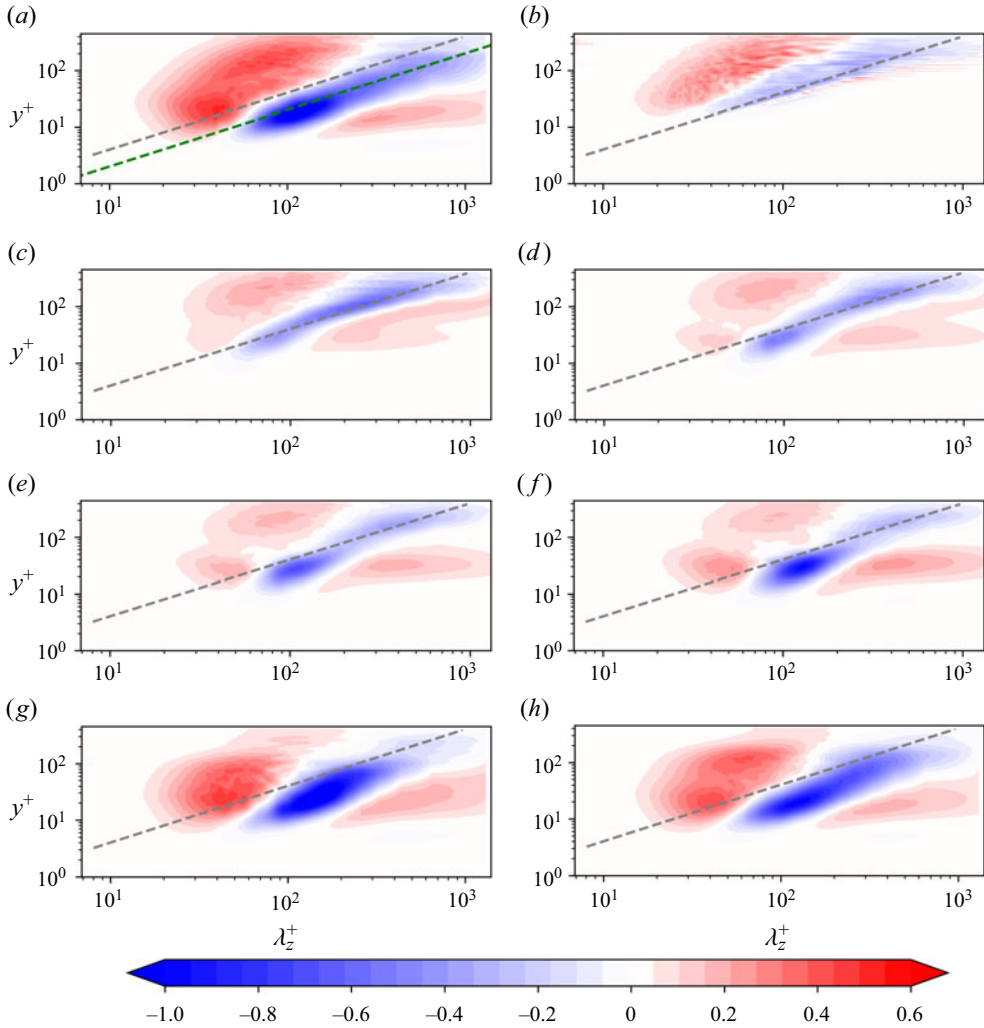


Figure 17. One-dimensional premultiplied interscale transport of the turbulent kinetic energy in the spanwise wavenumber direction ( $k_z y^+ t_{rkt}^+$ ) at various streamwise locations: (a) PCH-DNS; (b)  $x = 0h$ ; (c)  $x = 1.5h$ ; (d)  $x = 3h$ ; (e)  $x = 6h$ ; (f)  $x = 8h$ ; (g)  $x = 12h$ ; (h)  $x = 24h$ . The PCH-DNS data are shown in panel (a), while panels (b)–(h) represent the IOCH-DNS data. Here, the grey dashed line is at  $\lambda_z = 3y$  to indicate the cutoff spanwise wavelength and the green dashed line is at  $\lambda_z = 5y$ .

a spanwise wavelength of  $\lambda_z^+ \simeq 100$  and  $y^+ \simeq 15$ , which is equivalent to the spanwise spacing of near-wall streaks. Moreover, the inverse energy cascade is predominant only in the near-wall region for  $y^+ \leq 20$ , indicating that the near-wall cycle involves both forward and inverse energy cascades. The TKE produced at the integral length scale of energy-containing motions is transferred to the motions below the ridge  $\lambda_z = 3y$ , i.e. energy-cascade motions through the forward energy cascade.

The interscale TKE transport spectrum of the IOCH-DNS in figure 17(b) is largely positive since the energy-containing motions have been filtered out at the inflow. As the flow develops in the IOCH-DNS, the negative regions of  $t_{rkt}$  become active and align along the cutoff ridge  $\lambda_z = 3y$ , as shown in figure 17(c,d). Notably, the near-wall peak of the negative region gets stronger at a spanwise spacing of near-wall streaks,

i.e.  $\lambda_z^+ \simeq 100$ , which is consistent with the TKE production spectrum. Further, the TKE from the near-wall streaks is transferred to scales smaller and larger than the spanwise spacing of near-wall streaks through forward and inverse energy cascades, respectively. Unlike the PCH-DNS, the inverse cascade in the IOCH-DNS is not only active in the near-wall region for  $x < 6h$ . However, it spans over the entire buffer and log layer for  $y^+ \simeq 20 \sim 100$ , and the energy-containing motions at large scales with  $\lambda_z^+ \simeq 200 \sim 1000$  receive energy from the near-wall streaks,  $\lambda_z^+ \simeq 100$ , indicating the predominant role of the inverse energy cascade in recovering the energy-containing motions. The interscale transport  $k_z t_{r_{kt}}$  at  $x = 24h$  represents the PCH-DNS, as shown in figure 17(h). In summary, the  $t_{r_{kt}}$  spectrum of the IOCH-DNS revealed that the near-wall cycle involves both forward and inverse energy cascades, with the inverse cascade predominant in recovering energy-containing motions at large scales. The subsequent sections perform a component-wise analysis of the interscale energy transport to identify the velocity component associated with the inverse energy cascade of TKE in the IOCH-DNS.

### 3.9. Interscale transport of Reynolds stress

The premultiplied interscale transport of the streamwise Reynolds stress  $k_z t_{r_{uu}}$ , based on (2.10c) and (2.11), in the spanwise wavenumber direction is illustrated in figure 18. In the fully developed PCH-DNS  $k_z t_{r_{uu}}$  spectrum, a peak in the negative region is observed at  $\lambda_z^+ \simeq 100$  and  $y^+ \simeq 15$ , which corresponds to the near-wall streaks spacing, the dominant feature of streamwise velocity fluctuations, as shown in figure 18(a). The occurrence of the inverse energy transport in  $\langle u'^2 \rangle$  at  $y^+ \simeq 15$  is consistent with the turbulent channel flow DNS study of Lee & Moser (2019). In the IOCH-DNS, the interscale  $\langle u'^2 \rangle$  transport spectrum at the inflow is positive, indicating the filtering out of streaks at the inflow, as shown in figure 18(b). As the IOCH-DNS flow develops, the  $t_{r_{uu}}$  spectrum exhibits similar behaviour as the  $t_{r_{kt}}$  spectrum, as the inverse energy cascade occurs over the entire log-layer, and the near-wall peak of the negative iso-contour is amplified, as shown in figure 18(c–f). This indicates the interscale transfer of streamwise energy from the near-wall streaks to recover the energy-containing motions at large scales. Figure 18(h) shows the interscale transport  $k_z t_{r_{uu}}$  at  $x = 24h$ , depicting the fully developed PCH-DNS.

Figure 19 displays the premultiplied interscale transport of the wall-normal Reynolds stress  $k_z t_{r_{vv}}$ . In the fully developed PCH-DNS, the wall-normal energy does not exhibit any evidence of inverse energy cascade as the negative region is located at larger spanwise wavelengths  $\lambda_z^+ > 100$  than the positive region, which is at  $\lambda_z^+ < 100$ , as illustrated in figure 19(a). This finding is in agreement with the previous studies on turbulent channel flow (Lee & Moser 2019), turbulent boundary layers (Chan, Schlatter & Chin 2021) and turbulent Couette flows (Kawata & Tsukahara 2021).

In the IOCH-DNS, the interscale transport of the wall-normal energy decays until  $x = 8h$ , as shown in figure 19(c–f). This decay is consistent with the decay of the wall-normal velocity spectra of the IOCH-DNS, as reported in our previous study (Kannadasan *et al.* 2023). At  $x = 12h$ , the streaks re-establish and the streamwise vortices begin to recover (Kannadasan *et al.* 2023). Consequently,  $k_z t_{r_{vv}}$  becomes active, representing the forward energy cascade, which is similar to the fully developed PCH-DNS, as shown in figure 19(g).

Figure 20 depicts the premultiplied interscale transport of the spanwise Reynolds stress  $k_z t_{r_{ww}}$ . In the fully developed PCH-DNS, a clear inverse energy cascade of  $\langle w'^2 \rangle$  is observed in the buffer layer at a spanwise wavelength  $\lambda_z^+ > 300$ , as shown in figure 20(a). This observation is consistent with previous studies on channel flows (Lee & Moser 2019),

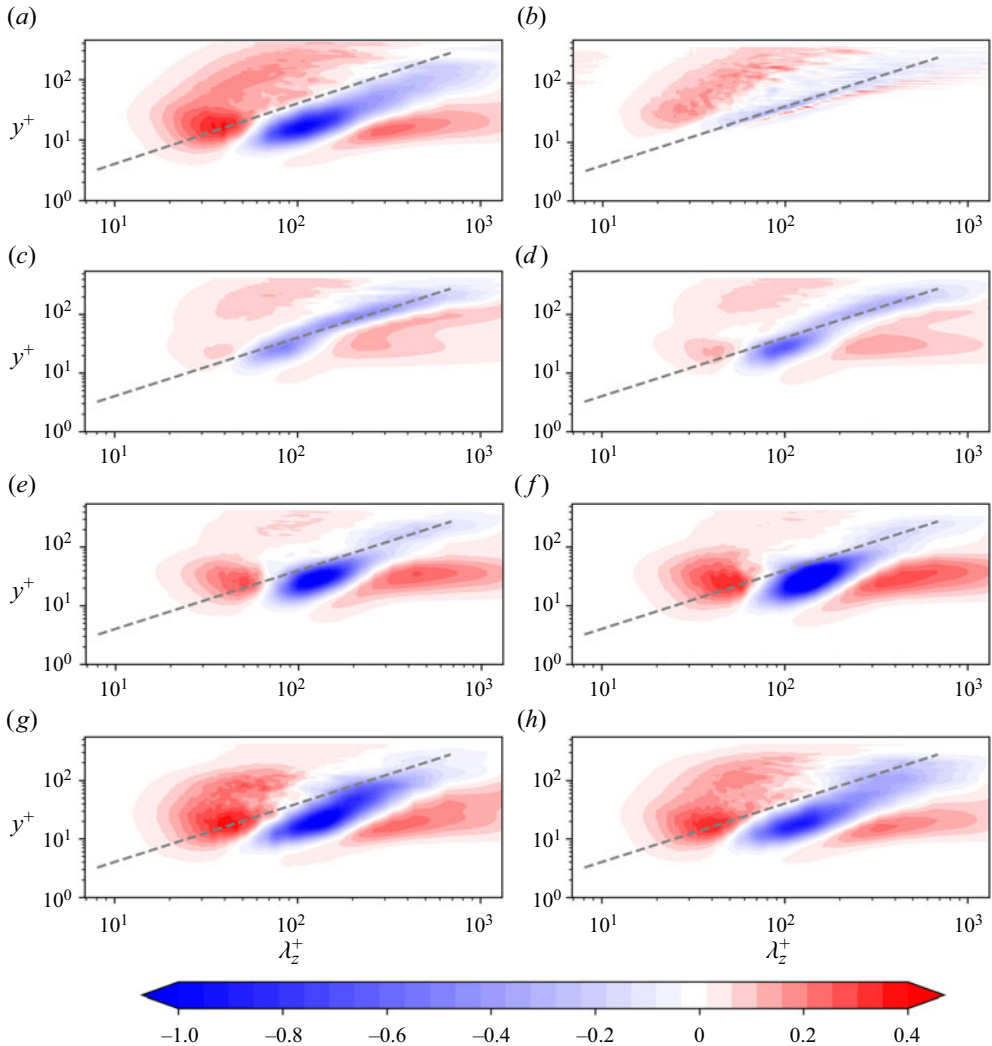


Figure 18. One-dimensional premultiplied interscale transport of the streamwise Reynolds stresses in the spanwise wavenumber direction ( $k_z y^+ r_{uu}^+$ ) at various streamwise locations: (a) PCH-DNS; (b)  $x = 0h$ ; (c)  $x = 1.5h$ ; (d)  $x = 3h$ ; (e)  $x = 6h$ ; (f)  $x = 8h$ ; (g)  $x = 12h$ ; (h)  $x = 24h$ . The PCH-DNS data are shown in panel (a), while panels (b)–(h) represent the IOCH-DNS data. Here, the grey dashed line is at  $\lambda_z^+ = 3y^+$  to indicate the cutoff spanwise wavelength.

turbulent boundary layers (Chan *et al.* 2021) and Couette flow (Kawata & Tsukahara 2021). However, in the IOCH-DNS, significant interscale transfer of spanwise energy is not observed until  $x = 12h$ , as demonstrated in figure 20(c–g). At  $x = 12h$ , when the streaks are re-established and the streamwise vortices recover, the negative iso-contour at  $\lambda_z^+ \simeq 100$  intensifies, as illustrated in figure 20(g). This behaviour suggests the significant gain of spanwise energy ( $\langle w'^2 \rangle$ ) through inter-component redistribution from  $\langle u'^2 \rangle$  to  $\langle w'^2 \rangle$ , as discussed in § 3.7. It is worth noting that the inverse cascade of spanwise energy is reactivated at  $x = 12h$  for  $\lambda_z^+ > 300$  and  $y^+ \simeq 10 \sim 30$ . Therefore, the interscale transport of Reynolds stresses in the spatially developing IOCH-DNS reveals that the inverse TKE

Interplay of scales of energy-containing motions

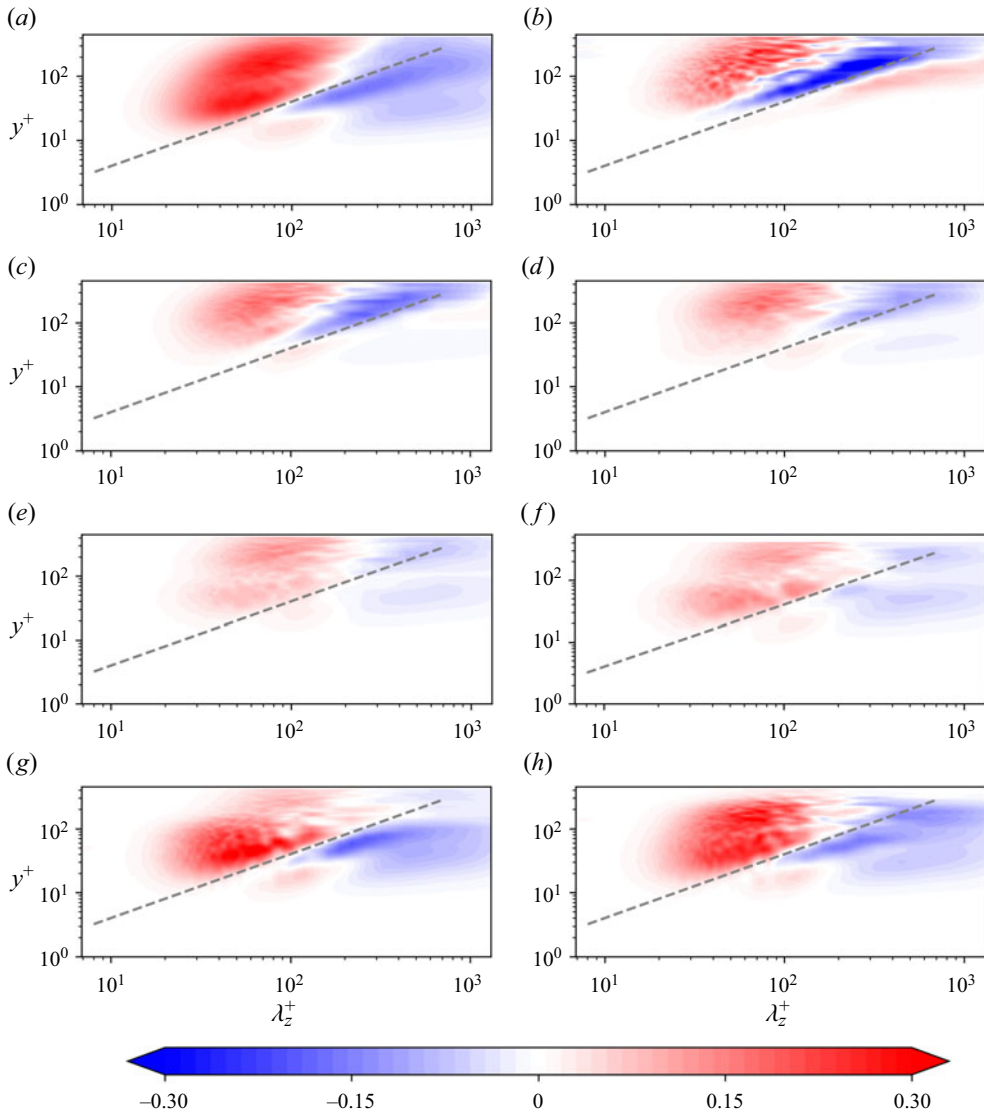


Figure 19. One-dimensional premultiplied interscale transport of the wall-normal Reynolds stresses in the spanwise wavenumber direction ( $k_z y^+ r_{rv}^+$ ) at various streamwise locations: (a) PCH-DNS; (b)  $x = 0h$ ; (c)  $x = 1.5h$ ; (d)  $x = 3h$ ; (e)  $x = 6h$ ; (f)  $x = 8h$ ; (g)  $x = 12h$ ; (h)  $x = 24h$ . The PCH-DNS data are shown in panel (a), while panels (b)–(h) represent the IOCH-DNS data. Here, the grey dashed line is at  $\lambda_z^+ = 3y^+$  to indicate the cutoff spanwise wavelength.

transport in the early stages of evolution in the IOCH-DNS is solely due to the streamwise velocity component, as the inverse energy cascade is absent near the wall in the  $\langle v'^2 \rangle$  and  $\langle w'^2 \rangle$  components for  $x < 12h$ . Furthermore, this inverse cascade of streamwise energy occurs from the near-wall streak's location ( $\lambda_z^+ \simeq 100$ ) to the energy-containing motions at large scales.

The results of the IOCH-DNS show that the inverse energy transfer of  $\langle w'^2 \rangle$  becomes active at  $x = 12h$  and is associated with the reactivation of streamwise vortices at larger

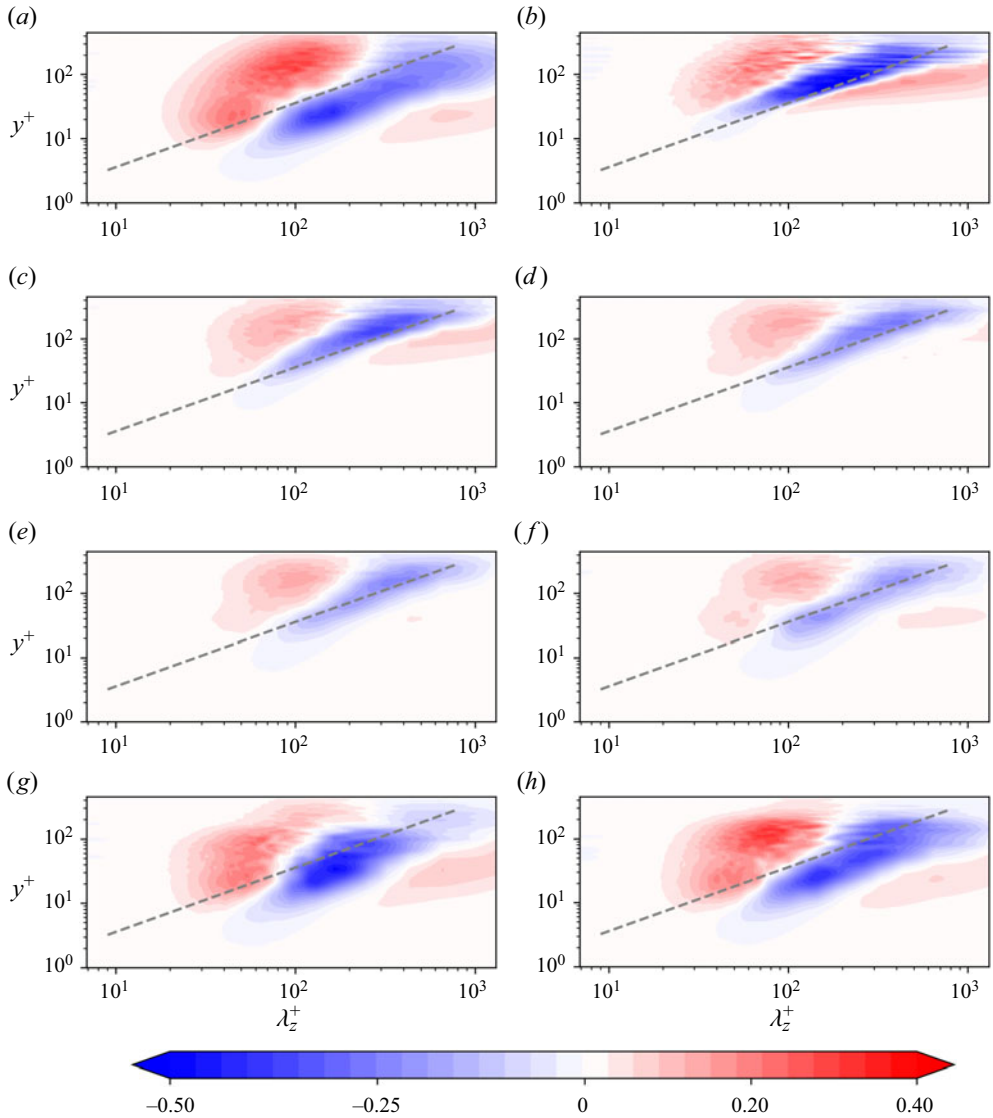


Figure 20. One-dimensional premultiplied interscale transport of the spanwise Reynolds stresses in the spanwise wavenumber direction ( $k_z y^+ t_{rw}^+$ ) at various streamwise locations: (a) PCH-DNS; (b)  $x = 0h$ ; (c)  $x = 1.5h$ ; (d)  $x = 3h$ ; (e)  $x = 6h$ ; (f)  $x = 8h$ ; (g)  $x = 12h$ ; (h)  $x = 24h$ . The PCH-DNS data are shown in panel (a), while panels (b)–(h) represent the IOCH-DNS data. Here, the grey dashed line is at  $\lambda_z = 3y$  to indicate the cutoff spanwise wavelength.

wavelengths for  $\lambda_z^+ \geq 300$ , which is a crucial part of the self-sustaining cycle. This observation is consistent with previous findings by Kawata & Tsukahara (2021) in Couette flow. The regeneration of streamwise vortices at large scales through an inverse interscale transfer of  $\langle w'^2 \rangle$  eventually leads to the regeneration of streaks by triggering turbulent energy production at large scales. This is clearly depicted in the spectra of TKE production in figure 13, where there is no TKE production at large scales ( $\lambda_z^+ \geq 300$ ) until  $x = 12h$ , the streamwise location where the inverse energy transfer of  $\langle w'^2 \rangle$  and streamwise vortices are reactivated. Consequently, in the spatial development of energy-containing

motions, the inverse interscale transport of spanwise turbulent energy may facilitate the TKE production at larger scales. In a related study, Hamba (2019) investigated the inverse interscale transport of spanwise energy and attempted to extract the corresponding vortical structure through conditional averaging. He found a longitudinal streamwise vortex accompanied by a shorter vortex located upstream, suggesting that the interactions between these vortices are responsible for the inverse energy cascade. Although the link between the structures found in his work and the regeneration process of the streamwise vortices in the self-sustaining cycle is still unclear, the inverse energy transfer of  $\langle w'^2 \rangle$  towards large wavelengths observed in the present study may also result from similar interactions between long vortices.

An insight supporting the correspondence between the interscale energy transport  $t_{ruu}$  and the self-sustaining process can be gained by decomposing  $t_{ruu}$ . The interscale flux of streamwise energy  $T_{ruu}$  can be expressed in a decomposed form, similar to (2.10c) as

$$\begin{aligned}
 T_{ruu} = & \underbrace{-2 \left\langle u'^{(S)} u'^{(S)} \frac{\partial u'^{(L)}}{\partial x} \right\rangle}_{T_{ruu}^1} \underbrace{-2 \left\langle u'^{(S)} v'^{(S)} \frac{\partial u'^{(L)}}{\partial y} \right\rangle}_{T_{ruu}^2} \underbrace{-2 \left\langle u'^{(S)} w'^{(S)} \frac{\partial u'^{(L)}}{\partial z} \right\rangle}_{T_{ruu}^3} \\
 & + 2 \underbrace{\left\langle u'^{(L)} u'^{(L)} \frac{\partial u'^{(S)}}{\partial x} \right\rangle}_{T_{ruu}^4} + 2 \underbrace{\left\langle u'^{(L)} v'^{(L)} \frac{\partial u'^{(S)}}{\partial y} \right\rangle}_{T_{ruu}^5} + 2 \underbrace{\left\langle u'^{(L)} w'^{(L)} \frac{\partial u'^{(S)}}{\partial z} \right\rangle}_{T_{ruu}^6}. \quad (3.4)
 \end{aligned}$$

Therefore, the interscale transport  $t_{ruu} = -\partial T_{ruu}(y, k_z)/\partial k_z$  can also be decomposed as

$$t_{ruu} = t_{ruu}^1 + t_{ruu}^2 + t_{ruu}^3 + t_{ruu}^4 + t_{ruu}^5 + t_{ruu}^6. \quad (3.5)$$

Figure 21 provides insights into the interscale energy transport  $t_{ruu}$  and its relation to the self-sustaining process. The various terms in (3.5) contributing to the interscale energy transport are shown at the near-wall streak location  $y^+ = 15$ . In the fully developed PCH-DNS, terms  $t_{ruu}^2$  and  $t_{ruu}^6$  are predominant, relating to the wall-normal and spanwise gradients of streamwise velocity fluctuations, respectively, as shown in figure 21(a). The wall-normal gradient of larger-scale structures ( $\partial u'^{(L)}/\partial y$ ), denoted as  $t_{ruu}^2$ , is shown to transfer energy from moderate to larger wavelengths, specifically from  $\lambda_z^+ \simeq 100$ , corresponding to the near-wall streaks location, to  $\lambda_z^+ > 200$ . This is consistent with the observations made in the  $t_{ruu}$  spectrum at  $y^+ = 15$  for  $\lambda_z^+ > 200$ , as shown in figure 18(a). Simultaneously,  $t_{ruu}^6$ , the spanwise gradient of smaller-scale structures ( $\partial u'^{(S)}/\partial z$ ), is noted to predominantly transfer energy from the streak location to further smaller scales,  $\lambda_z^+ < 60$ , while also supporting a substantial inverse cascade to larger scales,  $\lambda_z^+ \approx 200 \simeq 300$ .

In the spatially developing IOCH-DNS, the dominant term is  $t_{ruu}^6$ , which represents the effect of the spanwise velocity gradient by the smaller structures  $\partial u'^{(S)}/\partial z$ . As the flow develops, the  $t_{ruu}^6$  term becomes stronger and more dominant than the other interscale transport terms. Particularly, the  $t_{ruu}^6$  term is at negative maximum at  $\lambda_z^+ \simeq 100$  at  $x = 10h$ , the streamwise position where the regeneration of streamwise vortices occurs at larger wavelengths. At  $x = 12h$  in the IOCH-DNS, the contributions by various terms of (3.5) become similar to the PCH-DNS.

The dominance of the  $t_{ruu}^6$  term in the interscale streamwise energy transport at the near-wall streaks location of the IOCH-DNS is likely associated with the near-wall streak

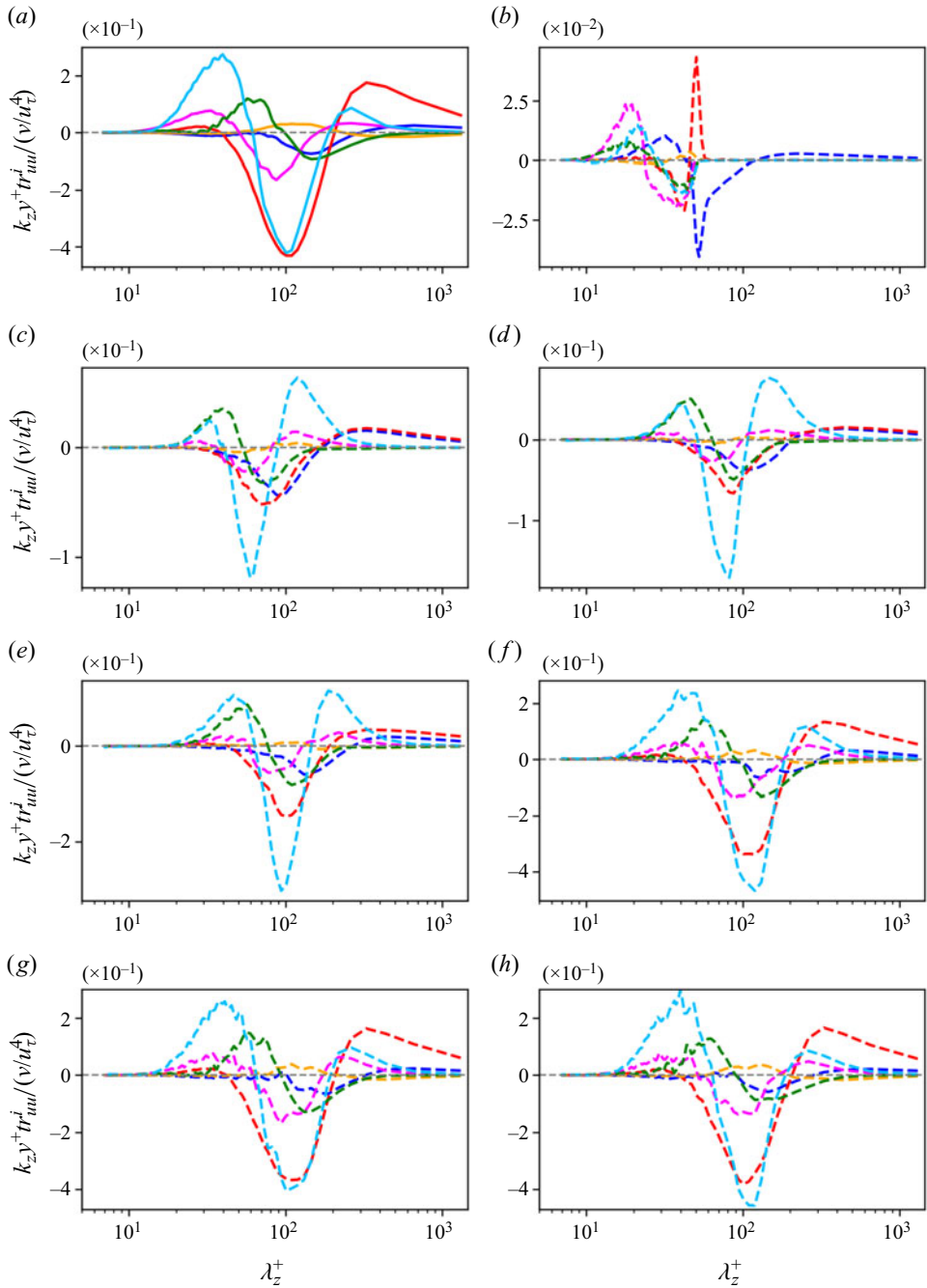


Figure 21. Comparison of various terms on the right-hand side of (3.5) at  $y^+ = 15$  and various streamwise locations: (a) PCH-DNS; (b)  $x = 0h$ ; (c)  $x = 1.5h$ ; (d)  $x = 3h$ ; (e)  $x = 6h$ ; (f)  $x = 10h$ ; (g)  $x = 12h$ ; (h)  $x = 24h$ . The PCH-DNS data are shown in panel (a), while panels (b)–(h) represent the IOCH-DNS data. Here, blue,  $t_{r_{uu}}^1$ ; red,  $t_{r_{uu}}^2$ ; yellow,  $t_{r_{uu}}^3$ ; magenta,  $t_{r_{uu}}^4$ ; green,  $t_{r_{uu}}^5$ ; cyan,  $t_{r_{uu}}^6$ .

instabilities in the reactivation of self-sustaining process. The spanwise variation of  $u'$  induced by the streaks can lead to inflectional instability (Swearingen & Blackwelder 1987; Hamilton *et al.* 1995; Jiménez & Pinelli 1999), which results in the formation of streamwise vortices that lift the near-wall low-speed streaks away from the wall and enhance the turbulent transport across the scales.

#### 4. Conclusions

This paper extends the previous investigation conducted by Kannadasan *et al.* (2023) on the spatial evolution of energy-containing motions, focusing on the interscale transport of TKE and Reynolds shear stress. The analysis yields three significant findings that enhance our understanding of the dynamics of energy-containing motions.

First, the examination of TKE production spectra reveals localised TKE production associated with the spacing of near-wall streaks. Moreover, there is a distinct amplification of near-wall streaks during the spatial evolution of energy-containing motions, particularly for streamwise locations up to  $x \leq 8h$ . This finding highlights the formation and intensification of streaks, providing insights into their role in the spatial evolution of energy-containing motions.

Second, the analysis of interscale transport of Reynolds stresses demonstrates a noteworthy inverse cascade of streamwise Reynolds stresses from near-wall streaks to the larger scales in the log-layer. This inverse streamwise energy cascade, driven by the spanwise variation of  $u'$ , indicates the inherent instability of amplified streaks. Third, the absence of an inverse cascade of spanwise energy for streamwise locations  $x \leq 8h$  and the quiescent behaviour of large-scale streamwise vortices suggest a potential relationship between the inverse cascade of spanwise energy and the regeneration of streamwise vortices at large-scales. This finding highlights the importance of an inverse spanwise energy cascade in reactivating the self-sustaining processes at large scales during the spatial development of energy-containing motions.

In summary, the findings of this study significantly contribute to our understanding of the dynamics of the spatial evolution of energy-containing motions. The formation and intensification of streaks in the early stages of evolution, the inverse cascade of streamwise Reynolds stress due to the spanwise variation of near-wall streaks and the potential role of spanwise energy cascade in the regeneration of streamwise vortices at large scales provide valuable insights into the self-sustaining processes occurring within the spatial evolution of energy-containing motions.

**Acknowledgements.** The authors would like to acknowledge the funding of this research by the Australian Research Council through a Discovery Grant. The authors also acknowledge the computational resources provided by the Pawsey Supercomputing Centre supported by the Australian and Western Australian Governments and the National Computational Infrastructure (NCI) supported by Australian Government through computational grants awarded by the National Computational Merit Allocation Scheme (NCMAS) funded by the Australian Government. Ezhilsabareesh Kannadasan gratefully acknowledges the support provided by a Monash Graduate Scholarship (MGS), Monash International Tuition Scholarship (MITS) and a Monash Postgraduate Publication Award (PPA).

**Declaration of interests.** The authors report no conflicts of interest.

#### Author ORCIDs.

 Ezhilsabareesh Kannadasan <https://orcid.org/0000-0003-1441-4311>;

 Callum Atkinson <https://orcid.org/0000-0003-3726-2103>;

 Julio Soria <https://orcid.org/0000-0002-7089-9686>.

## REFERENCES

- BAUER, C., VON KAMEKE, A. & WAGNER, C. 2019 Kinetic energy budget of the largest scales in turbulent pipe flow. *Phys. Rev. Fluids* **4** (6), 064607.
- BUTLER, K.M. & FARRELL, B.F. 1993 Optimal perturbations and streak spacing in wall-bounded turbulent shear flow. *Phys. Fluids A* **5** (3), 774–777.
- CHAN, C.I., SCHLATTER, P. & CHIN, R.C. 2021 Interscale transport mechanisms in turbulent boundary layers. *J. Fluid Mech.* **921**, A13.
- CHO, M., HWANG, Y. & CHOI, H. 2018 Scale interactions and spectral energy transfer in turbulent channel flow. *J. Fluid Mech.* **854**, 474–504.
- CIMARELLI, A., DE ANGELIS, E. & CASCIOLA, C.M. 2013 Paths of energy in turbulent channel flows. *J. Fluid Mech.* **715**, 436–451.
- CIMARELLI, A., DE ANGELIS, E., JIMÉNEZ, J. & CASCIOLA, C.M. 2016 Cascades and wall-normal fluxes in turbulent channel flows. *J. Fluid Mech.* **796**, 417–436.
- DOGAN, E., HEARST, R.J., HANSON, R.E. & GANAPATHISUBRAMANI, B. 2019 Spatial characteristics of a zero-pressure-gradient turbulent boundary layer in the presence of free-stream turbulence. *Phys. Rev. Fluids* **4** (8), 084601.
- FLORES, O. & JIMÉNEZ, J. 2006 Effect of wall-boundary disturbances on turbulent channel flows. *J. Fluid Mech.* **566**, 357–376.
- FLORES, O., JIMÉNEZ, J. & DEL ALAMO, J.C. 2007 Vorticity organization in the outer layer of turbulent channels with disturbed walls. *J. Fluid Mech.* **591**, 145–154.
- DE GIOVANETTI, M., HWANG, Y. & CHOI, H. 2016 Skin-friction generation by attached eddies in turbulent channel flow. *J. Fluid Mech.* **808**, 511–538.
- HAMBA, F. 2015 Turbulent energy density and its transport equation in scale space. *Phys. Fluids* **27** (8), 085108.
- HAMBA, F. 2019 Inverse energy cascade and vortical structure in the near-wall region of turbulent channel flow. *Phys. Rev. Fluids* **4**, 114609.
- HAMILTON, J.M., KIM, J. & WALEFFE, F. 1995 Regeneration mechanisms of near-wall turbulence structures. *J. Fluid Mech.* **287**, 317–348.
- HOYAS, S. & JIMÉNEZ, J. 2008 Reynolds number effects on the Reynolds-stress budgets in turbulent channels. *Phys. Fluids* **20** (10), 1–9.
- HUTCHINS, N. & MARUSIC, I. 2007 Evidence of very long meandering features in the logarithmic region of turbulent boundary layers. *J. Fluid Mech.* **579**, 1–28.
- HWANG, Y. 2015 Statistical structure of self-sustaining attached eddies in turbulent channel flow. *J. Fluid Mech.* **767**, 254–289.
- HWANG, Y. & COSSU, C. 2010 Self-sustained process at large scales in turbulent channel flow. *Phys. Rev. Lett* **105** (4), 044505.
- JIMÉNEZ, J. & MOIN, P. 1991 The minimal flow unit in near-wall turbulence. *J. Fluid Mech.* **225**, 213–240.
- JIMÉNEZ, J. & PINELLI, A. 1999 The autonomous cycle of near-wall turbulence. *J. Fluid Mech.* **389**, 335–359.
- KANNADASAN, E., ATKINSON, C. & SORIA, J. 2023 Spectral analysis of the evolution of energy-containing eddies. *J. Fluid Mech.* **955**, R1.
- KAWATA, T. & ALFREDSSON, P.H. 2018 Inverse interscale transport of the Reynolds shear stress in plane Couette turbulence. *Phys. Rev. Lett.* **120** (24), 244501.
- KAWATA, T. & TSUKAHARA, T. 2021 Scale interactions in turbulent plane Couette flows in minimal domains. *J. Fluid Mech.* **911**, A55.
- KIM, J. 2011 Physics and control of wall turbulence for drag reduction. *Phil. Trans. R. Soc. A* **369** (1940), 1396–1411.
- KIM, J., KLINE, S.J. & REYNOLDS, W.C. 1971 The production of turbulence near a smooth wall in a turbulent boundary layer. *J. Fluid Mech.* **50** (1), 133–160.
- KIM, J. & LIM, J. 2000 A linear process in wall-bounded turbulent shear flows. *Phys. Fluids* **12** (8), 1885–1888.
- KIM, J. & MOIN, P. 1985 Application of a fractional-step method to incompressible Navier–Stokes equations. *J. Comput. Phys.* **59** (2), 308–323.
- KLEBANOFF, P.S., TIDSTROM, K.D. & SARGENT, L.M. 1962 The three-dimensional nature of boundary layer instabilities. *J. Fluid Mech.* **12** (1), 1–34.
- KLINE, S.J., REYNOLDS, W.C., SCHRAUB, F.A. & RUNSTADLER, P.W. 1967 The structure of turbulent boundary layers. *J. Fluid Mech.* **30** (4), 741–773.
- LANDAHL, M.T. 1975 Wave breakdown and turbulence. *SIAM J. Appl. Maths* **28** (4), 735–756.
- LEE, M. & MOSER, R.D. 2019 Spectral analysis of the budget equation in turbulent channel flows at high Reynolds number. *J. Fluid Mech.* **860**, 886–938.

## *Interplay of scales of energy-containing motions*

- LOZANO-DURÁN, A. & BAE, H.J. 2019 Characteristic scales of Townsend's wall-attached eddies. *J. Fluid Mech.* **868**, 698–725.
- LOZANO-DURÁN, A., HACK, M.J.P. & MOIN, P. 2018 Modeling boundary-layer transition in direct and large-eddy simulations using parabolized stability equations. *Phys. Rev. Fluids* **3**, 023901.
- MATHIS, R., HUTCHINS, N. & MARUSIC, I. 2009 Large-scale amplitude modulation of the small-scale structures in turbulent boundary layers. *J. Fluid Mech.* **628**, 311–337.
- MIZUNO, Y. 2016 Spectra of energy transport in turbulent channel flows for moderate Reynolds numbers. *J. Fluid Mech.* **805**, 171–187.
- MOTOORI, Y. & GOTO, S. 2021 Hierarchy of coherent structures and real-space energy transfer in turbulent channel flow. *J. Fluid Mech.* **911**, A27.
- PERRY, A.E. & CHONG, M.S. 1982 On the mechanism of wall turbulence. *J. Fluid Mech.* **119**, 173–217.
- RICHARDSON, L.F. 1922 *Weather Prediction by Numerical Process*. Cambridge University Press.
- SCHOPPA, W. & HUSSAIN, F. 2002 Coherent structures in turbulence. *J. Fluid Mech.* **453**, 57–108.
- SWEARINGEN, J.D. & BLACKWELDER, R.F. 1987 The growth and breakdown of streamwise vortices in the presence of a wall. *J. Fluid Mech.* **182**, 255–290.
- TOWNSEND, A.A. 1980 *The Structure of Turbulent Shear Flow*. Cambridge University Press.
- WALEFFE, F. 1995 Transition in shear flows. Nonlinear normality versus non-normal linearity. *Phys. Fluids* **7** (12), 3060–3066.
- WALEFFE, F. 1997 On a self-sustaining process in shear flows. *Phys. Fluids* **9** (4), 883–900.